Vector photon-magnon-phonon coherence in a polarized microwave driven cavity magnomechanical system

Jia-Xin Peng,[1,*] Akash Kundu,[2,3,†] Zeng-Xing Liu,[4] Atta ur Rahman,[5] Naeem Akhtar,[6] and M. Asjad[7,‡]

[1]*Quantum Institute for Light and Atoms, State Key Laboratory of Precision Spectroscopy, Department of Physics, School of Physics and Electronic Science, East China Normal University, Shanghai 200062, China*

[2]*Institute of Theoretical and Applied Informatics, Polish Academy of Sciences, Gliwice, Poland*

[3]*Joint Doctoral School, Silesian University of Technology, Gliwice, Poland*

[4]*School of Electronic Engineering & Intelligentization, Dongguan University of Technology, Dongguan, Guangdong 523808, China*

[5]*School of Physical Sciences, University of Chinese Academy of Sciences, Yuquan Road 19A, Beijing 100049, China*

[6]*Department of Physics, Jiangsu University, Zhenjiang 212013, China*

[7]*Mathematics Department, Khalifa University of Science and Technology, Abu Dhabi 127788, United Arab Emirates*

(Received 12 October 2023; revised 19 January 2024; accepted 23 January 2024; published 14 February 2024)

Polarization is a significant vector property of the light field that has been widely applied in various fields of modern optical sciences. In this paper, we introduce the concept of polarization into the cavity-magnomechanical system as a platform for studying quantum coherence in the vector regime. Interestingly, we find that quantum coherence can be flexibly and continuously controlled by adjusting the polarization angle of the optical polarizer and implementing coherent switching and role reversal between the two types of photon-magnon-phonon coherences for the transverse electric and transverse magnetic modes. More importantly, this coherent conversion characteristic of quantum coherence exhibits strong robustness to environmental temperature and dissipation channels. In practice, this ability to switch macroscopic quantum coherence would provide another degree of freedom for quantum information science based on the cavity-magnomechanical system. In addition, the experimental feasibility of the polarization-controlled quantum coherence is evaluated, and the strategy for detecting vector quantum coherence is discussed briefly.

DOI: 10.1103/PhysRevB.109.064412

I. INTRODUCTION

Quantum coherence is the basic characteristic of quantum states and the objective embodiment of the quantum superposition principle [1–3]. Having a long history, quantum coherence phenomenon involves affecting both macroscopic scales like superfluidity and superradiance, along with superconductivity and microscopic scales such as atomic, and qubits in nature [4]. In recent times, quantum coherence has been considered a physical resource [4–6] and has been shown to be essential for quantum information theory [7–10], quantum thermodynamics [11–15], quantum biology [16,17], quantum optics [18–21], and quantum metrology [22,23]. Especially with the proposal of quantifying quantum coherence [1,2], researchers' enthusiasm for this field has been greatly activated, and a large number of new research results have emerged. It is worth mentioning that a method for quantifying the quantum coherence of an infinite-dimensional bosonic system based on the relative entropy has been established [24,25]. This not only promotes the research of quantum coherence in macroscopic systems but also deepens the understanding of the boundary between classical and quantum worlds. Very recently, quantum coherence at the macroscopic level has been studied in various physical systems, including Bose-Einstein condensates [26,27], Josephson junctions [28–30], optomechanical systems [31–34], whispering-gallery-mode resonator systems [35,36], Laguerre-Gaussian rotating cavity [37], and more. Even more exciting is that macroscopic quantum coherence has been experimentally confirmed [38,39], thus making the first step in applying quantum coherence to practical applications.

Vector beams are known for their capability to control light by the manipulation of polarization, which plays a crucial role in both fundamental scientific investigations and practical implementations in the fields of optics and photonics [40–42]. A skillful control of the polarization of vector beams can offer effective ways to achieve various applications in material processing [43,44], optical imaging [45–47], data storage [48], and sensing [49], while it can also enhance the nonlinear optical effects [50]. Impressively, the nanotechnology and vectorial optical fields have led to unique light-matter interactions arising from the interplay between the spatial distribution and polarization of a vector beam mediated via a suitably structured optical media [51,52]. Recently, Xiong *et al.* proposed a vector cavity optomechanical system [53]. Unlike conventional scalar light sources that have been utilized to gain control in cavity optomechanical systems, in vector cavity optomechanics, the optomechanical control is

*52204700007@stu.ecnu.edu.cn
†akundu@iitis.pl
‡asjad_qau@yahoo.com

realized by the polarization of the optical field. They found that, based on this system, the underlying physical process of optomechanically induced transparency can be easily identified. Subsequently, Li *et al.* studied vector optomechanical entanglement in such a vector cavity optomechanical system [54]. This study is of great significance for building the efficient quantum communication in vectorial optomechanical device.

In the past few years, the yttrium iron garnet (YIG) sphere, a class of ferrimagnetic systems with high-spin density and low loss, has attracted notable interest in the field of quantum information sciences [55–58]. Some studies have shown that the excited magnon modes in the YIG sphere can be coupled with microwave photons. Naturally, this microwave-magnon coupling provides an opportunity for the birth of magnon cavity quantum electrodynamics [59–62]. More importantly, with the experimental implementation of the photon-magnon-phonon interactions [58], this field has received considerable attention. In 2018, Li *et al.* presented a full quantum theory of the cavity-magnomechanical system and studied magnon-photon-phonon entanglement [63]. This study has opened a subfield of studying quantum entanglement and opened the door to the investigation of macroscopic quantum phenomena in quantum magnonics [56]. The hybrid cavity-magnomechanical system has received increasing attention, resulting in significant achievements such as preparing macroscopic quantum states [64–67], nonclassical states of microwave fields [68–70], ground-state cooling of the magnetic resonator [71,72], bistability [73–77], magnon blockade [78–82], optical/magnon response or laser [83–91], quantum steering [92,93], building quantum networks and quantum information science [56,94], storage and conversion of quantum states [95], quantum sensing [96], chiral and topological [88,97–99], and quantum correlations between various systems and magnon [100–111].

The above extensive studies demonstrate the flourishing development of various research branches in cavity magnetic field. It is worth mentioning that, although macroscopic quantum entanglement is extensively studied in cavity-magnomechanical systems, much less effort has been devoted to investigate quantum coherence in these systems. Motivated by this, here we focus on studying the quantum coherence phenomenon in a cavity-magnomechanical system. This is crucial for clarifying the relationship between macroscopic quantum entanglement and quantum coherence. A recent interesting work investigated the second-order quantum coherence of photons and magnons, respectively [112]. However, this work does not study the quantum coherence between photons and magnons. Particularly, to the best of our knowledge, the study of the vector cavity-magnomechanical system has not been reported until now. From a theoretical and experimental perspective, the fusion of polarization with cavity-magnomechanical systems appears to hold significant promise as a research frontier. This serves as the driving force for our work.

In the present paper, we propose a vector cavity-magnomechanical system in which the cavity modes are driven by a polarized microwave. Based on this system, the macroscopic quantum coherence is studied in the vector regime, and we show that the coherent switch of the quantum photon-magnon-phonon coherence can be implemented by manipulating the polarization angle of optical polarizer. This result may have significant implications for establishing vectorial quantum networks based on cavity-magnomechanical systems. It is worth mentioning that this optical modulation achieved through polarization manipulation can also be applied to identify the underlying physical process and control of magnomechanically induced transparency [113], or to investigate other cavity-magnomechanical-based related effects. In addition to polarization angle, we also explore the dependence of the photon-magnon-phonon coherence on the microwave driving power, drive magnetic field, ambient temperature, dissipation effects, microwave-magnon coupling rate, and single-magnon magnomechanical coupling strength. Finally, we discuss the feasibility of the experiment, and an all-optical measurement strategy is suggested for detecting the polarization-controlled quantum coherence.

The structure of this paper is as follows. In Sec. II, we introduce the theoretical model and Hamiltonian for the polarization-driven cavity-magnomechanical system in detail. In Sec. III, we exploit the Heisenberg-Langevin method to describe the dynamics of the system, and the basic theory of quantifying Gaussian quantum coherence is given. In Sec. IV, we first explore the stable parameter regions of the system, and then numerically study the effects of the polarization angle and other physical factors related with quantum coherence. The explanation of the experimental feasibility and detecting scheme for the photon-magnon-phonon coherences with respect to the transverse electric (TE) and transverse magnetic (TM) modes are illustrated in Sec. V. Finally, we discuss the relevant physical insights of the photon-magnon-phonon coherence and then summarize this article in Sec. VI. The stability conditions of the system are given in the Appendix.

II. THEORETICAL MODEL AND HAMILTONIAN

We consider a polarized-microwave-driven cavity-magnomechanical system that contains an optical polarizer, a three-dimensional (3D) microwave copper cavity, and a YIG sphere (250 μm diameter), as schematically shown in Fig. 1(a). For the 3D microwave cavity, one can construct a group of unit orthogonal basis vectors of polarization, physically corresponding to TE [$|\vec{e}_{\updownarrow}\rangle$, vertically] and TM [$|\vec{e}_{\leftrightarrow}\rangle$, horizontally] modes, satisfying that $\langle\vec{e}_{\updownarrow(\leftrightarrow)}|\vec{e}_{\updownarrow(\leftrightarrow)}\rangle = 1$ and $\langle\vec{e}_{\updownarrow(\leftrightarrow)}|\vec{e}_{\leftrightarrow(\updownarrow)}\rangle = 0$ (orthogonal cavity modes) [53]. Therefore, any unit vector can be conveniently represented as $|\vec{e}\rangle = \cos\theta|\vec{e}_{\updownarrow}\rangle + \sin\theta|\vec{e}_{\leftrightarrow}\rangle$, indicating that the spatial distribution of a linearly polarized microwave field can be flexibly controlled by adjusting the polarization angle θ. In particular, the concepts of TE and TM can well corresponded to the effect of the polarization rotation induced by curved waveguides in whispering-gallery-mode microresonator, and what's exciting is that they have been experimentally confirmed [114]. On the other hand, the YIG sphere placed inside the microwave cavity will excite a large number of magnon modes under the action of a static-uniform bias magnetic field H_B in the Z direction and a driving magnetic field. As the magnons are excited, the magnetization of the YIG sphere will change, leading to the mechanical deformation of the YIG sphere [56–58,63]. This is the

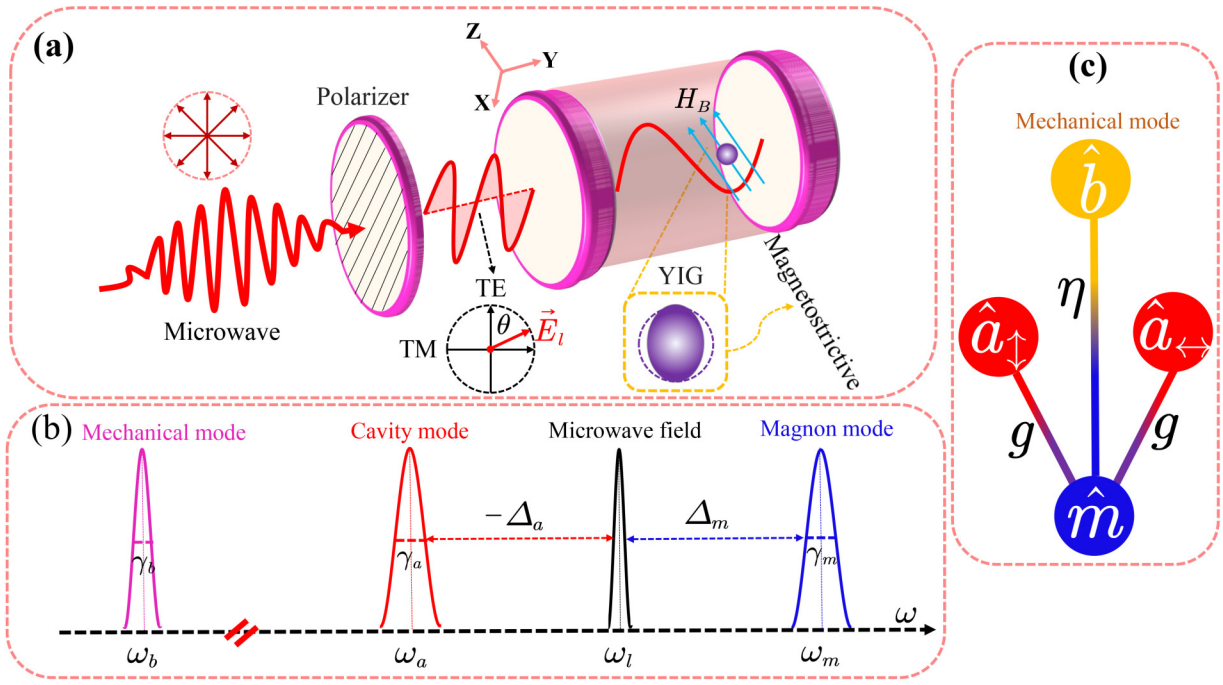

FIG. 1. (a) The diagrammatic representation of the polarized-microwave-driven cavity-magnomechanical system. The 3D copper cavity is driven by a polarized-microwave with power P_l and frequency ω_l, inducing the orthogonal cavity modes $\hat{a}_\updownarrow$ (TE) and $\hat{a}_\leftrightarrow$ (TM) in the cavity. In addition, applying a static-uniform bias magnetic field H_B in the Z direction and a driving magnetic field B_0 (not shown) to YIG sphere excites a large number of magnon modes. The deformation of YIG sphere also leads to mechanical modes owing to themagnetostrictive effect. Accordingly, there are two types of interactions within the polarized-microwave-driven cavity-magnomechanical system, namely, the magnetic-dipole interaction between the orthogonal cavity modes and the magnon, as well as the magnomechanical coupling between the magnon and the phonon mode. (b) Frequency spectrums and linewidths of modes in the system. (c) The schematic diagram of interactions among subsystems in the cavity-magnomechanical system.

so-called magnetostrictive effect, which induces mechanical (phonon) modes. As a result, the magnon and phonon modes exhibit dispersive coupling (a radiation pressurelike interaction) similar to optomechanics. In addition, there is a beam-splitter-like coupling between the microwave cavity modes and magnon mode due to magnetic-dipole interaction. Combining these fragments above, the total Hamiltonian of the polarized-microwave-driven cavity-magnomechanical system can be written as [53,63] (we set $\hbar = 1$ hereafter)

$$\begin{aligned}\hat{H} =& \omega_a \sum_{j=\updownarrow,\leftrightarrow} \hat{a}_j^\dagger \hat{a}_j + \omega_m \hat{m}^\dagger \hat{m} + \frac{\omega_b}{2}(\hat{p}^2 + \hat{q}^2) \\ &+ g \sum_{j=\updownarrow,\leftrightarrow} (\hat{m}^\dagger \hat{a}_j + \hat{m}\hat{a}_j^\dagger) + \eta \hat{m}^\dagger \hat{m}\hat{q} \\ &+ i \sum_{j=\updownarrow,\leftrightarrow} \varepsilon_j (\hat{a}_j^\dagger e^{-i\omega_l t} - \hat{a}_j e^{i\omega_l t}) \\ &+ i\Omega_l (\hat{m}^\dagger e^{-i\omega_l t} - \hat{m} e^{i\omega_l t}), \end{aligned} \tag{1}$$

where $\hat{a}_j^\dagger(\hat{a}_j)$ are the bosonic creation (annihilation) operators of the orthogonal microwave cavity modes with frequency ω_a ($[\hat{a}_j, \hat{a}_j^\dagger] = 1$); $\hat{m}^\dagger(\hat{m})$ are the bosonic creation (annihilation) operators for the magnon mode with frequency $\omega_m([\hat{m}, \hat{m}^\dagger] = 1)$, in which $\omega_m = \gamma_e H_B$, and $\gamma_e/2\pi = 28$ GHz denotes the gyromagnetic ratio for electrons [56,57]; $\hat{q}$ and $\hat{p}$, respectively, denote the dimensionless displacement and momentum operators of the mechanical mode with frequency ω_b ($[\hat{q}, \hat{p}] = i$). Specifically, the first three terms represent the Hamiltonian of the orthogonal microwave cavity modes, magnon and phonon mode, respectively. The fourth term refers to the magnetic-dipole interaction between the orthogonal microwave cavity modes and magnon, where g is the microwave-magnon coupling strength. The fifth term represents the radiation pressurelike interaction coupling between magnon and phonon modes, in which η is magnomechanical coupling rate. Note that this item only becomes significant when the mean magnon number in the system is large, owing to η being typically small. The last two items refer to the polarization microwave driving of the orthogonal cavity field and the direct driving of the YIG sphere, respectively. $E_l = \sqrt{2\gamma_a P_l/\omega_l}$ is the amplitude of polarized-microwave, where γ_a, P_l, and ω_l refer to the orthogonal cavity mode decay rate, power, and frequency of polarization microwave driving, respectively. $\varepsilon_\updownarrow = E_l \cos\theta$ and $\varepsilon_\leftrightarrow = E_l \sin\theta$ are the projections of E_l onto the TE and TM modes, respectively. $\Omega_l = \frac{\sqrt{5}}{4}\gamma_e\sqrt{N}B_0$ represents the coupling rate between the magnon and the drive magnetic field with amplitude B_0 and frequency ω_l, where N is the total number of spins in the YIG sphere ($N \simeq 3.5\times10^{16}$ for a 250-μm-diameter YIG sphere) [63,66]. It is worth mentioning that the wavelength of the microwave is much larger than the size of the YIG sphere, so the radiation pressure effect is not considered (the wavelength of microwave with a frequency of 10 GHz is approximately 3 cm $\gg$ 250 μm). Furthermore, in Eq. (1) we have neglected the Kerr effect of the magnon and adopted the assumption

of magnon low-lying excitations [56–58,63]. As such, in the discussion in Fig. 5, we also analyzed the validity of the model.

Equation (1) contains the time-dependent term, which is not conducive to solving the model. To eliminate the time factor, we introduce the transformation $\hat{U}(t) = e^{-i\omega_l t(\hat{a}_\updownarrow^\dagger \hat{a}_\updownarrow + \hat{a}_\leftrightarrow^\dagger \hat{a}_\leftrightarrow + \hat{m}^\dagger \hat{m})}$, i.e., the rotating frame with respect to microwave driving. As a consequence of this transformation, the Hamiltonian $\hat{H}$ can be written as [115]

$$\begin{aligned}\hat{H}_r &= \hat{U}(t)\hat{H}\hat{U}^\dagger(t) - i\hat{U}(t)\frac{d\hat{U}^\dagger(t)}{dt} \\ &= \Delta_a \sum_{j=\updownarrow,\leftrightarrow} \hat{a}_j^\dagger \hat{a}_j + \Delta_m \hat{m}^\dagger \hat{m} + \frac{\hbar\omega_b}{2}(\hat{p}^2 + \hat{q}^2) \\ &\quad + g \sum_{j=\updownarrow,\leftrightarrow} (\hat{m}^\dagger \hat{a}_j + \hat{m}\hat{a}_j^\dagger) + \eta \hat{m}^\dagger \hat{m}\hat{q} \\ &\quad + i \sum_{j=\updownarrow,\leftrightarrow} \varepsilon_j (\hat{a}_j^\dagger - \hat{a}_j) + i\Omega_l(\hat{m}^\dagger - \hat{m}), \end{aligned} \tag{2}$$

where $\Delta_a = \omega_a - \omega_l$ ($\Delta_m = \omega_m - \omega_l$) is the detuning of microwave driving from the orthogonal cavity (magnon) mode. We can clearly see that the transformed Hamiltonian is no longer dependent on time. This greatly facilitates the solution of the system.

III. ANALYSIS: QUANTUM DYNAMICS AND GAUSSIAN COHERENCE

A. Dynamics analysis

In this subsection, we will describe the dynamic behavior of the system. Note also that all modes, except for their own linewidth, are inevitably influenced by external environments (or bath), known as the fluctuation-dissipation theorem. In this sense, what we essentially study is a polarized-driven-dissipative cavity-magnomechanical system. A powerful tool for describing the time dynamics of open nonlocal systems is the quantum master equation or its equivalent Heisenberg-Langevin equation [116]. We adopt the latter for our current paper, which is the most commonly used method to handle continuous variable systems. According to the Heisenberg-Langevin method, the dynamics of the system can be described by the following nonlinear equations, i.e.:

$$\begin{aligned}\frac{d\hat{a}_j}{dt} &= -(i\Delta_a + \gamma_a)\hat{a}_j - ig\hat{m} + \varepsilon_j + \sqrt{2\gamma_a}\hat{a}_j^{\text{in}}, (j = \updownarrow, \leftrightarrow), \\ \frac{d\hat{m}}{dt} &= -[i(\Delta_m + \eta\hat{q}) + \gamma_m]\hat{m} - ig\sum_{j=\updownarrow,\leftrightarrow} \hat{a}_j + \Omega_l + \sqrt{2\gamma_m}\hat{m}^{\text{in}}, \\ \frac{d\hat{q}}{dt} &= \omega_b \hat{p}, \frac{d\hat{p}}{dt} = -\omega_b\hat{q} - \gamma_b\hat{p} - \eta\hat{m}^\dagger\hat{m} + \hat{\xi}, \end{aligned} \tag{3}$$

where γ_m and γ_b refer to the decay rates of magnon and phonon modes, respectively; $\hat{a}_j^{\text{in}}$, $\hat{m}^{\text{in}}$, and $\hat{\xi}$ represent the input noise operators induced by the environments. These noise operators have zero mean values, namely, $\langle \hat{a}_j^{\text{in}} \rangle = \langle \hat{m}^{\text{in}} \rangle = \langle \hat{\xi} \rangle$, and satisfying that the correlation functions $\langle \hat{a}_j^{\text{in}}(t_1)\hat{a}_j^{\text{in}^\dagger}(t_2)\rangle = [N_a(\omega_a) + 1]\delta(t_1 - t_2)$, $\langle \hat{m}^{\text{in}}(t_1)\hat{m}^{\text{in}^\dagger}(t_2)\rangle = [N_m(\omega_m) + 1]\delta(t_1 - t_2)$ and $\langle \hat{\xi}(t_1)\hat{\xi}(t_2)\rangle = \frac{\gamma_b}{\omega_b}\int \frac{d\omega}{2\pi} e^{-i\omega(t_1-t_2)}\omega[\coth(\frac{\omega}{2k_BT}) + 1]$ (non-Markovian correlation) [117], indicating that the orthogonal cavity modes and magnon are affected by the thermal noise, while the mechanical mode is affected by the Brownian noise. These correlation functions represent the properties of the environment and are used to calculate the diffusion matrix later. In addition, $N_k(\omega_k) = [\exp(\omega_k/k_BT) - 1]^{-1}$ ($k = a, m, b$) are mean thermal excitation numbers for various modes, where k_B denotes the Boltzmann constant and T is the environment temperature. Particularly, the quantum correlation effects are well achieved when the mechanical mode has a large mechanical quality factor, i.e., $Q_b = \omega_b/\gamma_b \gg 1$. In this limit, one can obtain $\langle \hat{\xi}(t_1)\hat{\xi}(t_2) + \hat{\xi}(t_2)\hat{\xi}(t_1)\rangle/2 \simeq \gamma_b[2N_b(\omega_b) + 1]\delta(t_1 - t_2)$ (Markovian process) [117], corresponding to a white noise input with δ correlation function. Another thing to note is that the correlation function for cavity modes is different from the field of optomechanics, where $N_a(\omega_a)$ can be ignored. This is because the order of magnitude of $N_a(\omega_a)$ and $N_b(\omega_a)$ in the microwave frequency band is consistent and thus cannot be ignored.

We assume that relatively strong driving is performed on the orthogonal cavity modes and YIG sphere, meaning that all modes have a large steady-state value. As such, the linearization approximation can be safely used, namely, $\hat{\Pi} := \langle\hat{\Pi}\rangle + \delta\hat{\Pi}$ ($\hat{\Pi} = \hat{a}_{\updownarrow,\leftrightarrow}, \hat{m}, \hat{q}, \hat{p}$) [100–111]. Here, $\langle\hat{\Pi}\rangle$ and $\delta\hat{\Pi}$ refer to the steady-state values and quantum fluctuations, respectively (the steady-state value is much larger than its fluctuation). Inserting linearization approximation into Eq. (3), we can obtain a set of equations for steady-state values and quantum fluctuation operators. The steady-state values for each mode read

$$\langle \hat{a}_j \rangle = \frac{\varepsilon_j - ig\langle\hat{m}\rangle}{i\Delta_a + \gamma_a}, \quad (j = \updownarrow, \leftrightarrow), \tag{4a}$$

$$\langle \hat{p} \rangle = 0, \langle \hat{q} \rangle = \frac{-\eta|\langle\hat{m}\rangle|^2}{\omega_b}, \tag{4b}$$

$$\langle \hat{m} \rangle = \frac{\Omega_l(i\Delta_a + \gamma_a) - ig\sum_{j=\updownarrow,\leftrightarrow}\varepsilon_\updownarrow}{(i\tilde{\Delta}_m + \gamma_m)(i\Delta_a + \gamma_a) + 2g^2}, \tag{4c}$$

where $\tilde{\Delta}_m = \Delta_m + \eta\langle\hat{q}\rangle$ is the effective magnon detuning in the presence of magnomechanical coupling. Note that the above equations may have multiple steady-state solutions, that is, the phenomenon of multistability, for instance, a univariate cubic equation regarding $|\langle\hat{m}\rangle|^2$. We declare here the parameters used in subsequent numerical simulations only give unique steady-state solutions for the system. This, in turn, imposes another constraint on the driving strength.

Further, we define the quadrature fluctuations of modes: $\delta\hat{X}_j = (\delta\hat{a}_j + \delta\hat{a}_j^\dagger)/\sqrt{2}$, $\delta\hat{Y}_j = (\delta\hat{a}_j - \delta\hat{a}_j^\dagger)/i\sqrt{2}$ ($j = \updownarrow, \leftrightarrow$), $\delta\hat{Q} = (\delta\hat{m} + \delta\hat{m}^\dagger)/\sqrt{2}$, and $\delta\hat{P} = (\delta\hat{m} - \delta\hat{m}^\dagger)/i\sqrt{2}$. The corresponding noise quadrature operators are $\delta\hat{X}_j^{\text{in}} = (\delta\hat{a}_j^{\text{in}} + \delta\hat{a}_j^{\text{in}^\dagger})/\sqrt{2}$, $\delta\hat{Y}_j^{\text{in}} = (\delta\hat{a}_j^{\text{in}} - \delta\hat{a}_j^{\text{in}^\dagger})/i\sqrt{2}$, $\delta\hat{Q}^{\text{in}} = (\delta\hat{m}^{\text{in}} + \delta\hat{m}^{\text{in}^\dagger})/\sqrt{2}$, and $\delta\hat{P}^{\text{in}} = (\delta\hat{m}^{\text{in}} - \delta\hat{m}^{\text{in}^\dagger})/i\sqrt{2}$ [100–111]. One then can obtain the equation for quantum fluctuation operators (linearized quantum Langevin equations),

given by

$$\frac{d\hat{\Phi}(t)}{dt} = \mathcal{A}\hat{\Phi}(t) + \hat{n}(t), \tag{5}$$

where $\hat{\Phi}(t) = (\delta\hat{X}_{\updownarrow}, \delta\hat{Y}_{\updownarrow}, \delta\hat{X}_{\leftrightarrow}, \delta\hat{Y}_{\leftrightarrow}, \delta\hat{Q}, \delta\hat{P}, \delta\hat{q}, \delta\hat{p})^{\mathrm{T}}$ is the quadrature fluctuation vector; $\hat{n}(t) = (\sqrt{2\gamma_a}\delta\hat{X}_{\updownarrow}^{\mathrm{in}}, \sqrt{2\gamma_a}\delta\hat{Y}_{\updownarrow}^{\mathrm{in}}, \sqrt{2\gamma_a}\delta\hat{X}_{\leftrightarrow}^{\mathrm{in}}, \sqrt{2\gamma_a}\delta\hat{Y}_{\leftrightarrow}^{\mathrm{in}}, \sqrt{2\gamma_m}\delta\hat{Q}^{\mathrm{in}}, \sqrt{2\gamma_m}\delta\hat{P}^{\mathrm{in}}, 0, \hat{\xi})^{\mathrm{T}}$ is the input noises vector, and the drift matrix has the form

$$\mathcal{A} = \begin{bmatrix} -\gamma_a & \Delta_a & 0 & 0 & 0 & g & 0 & 0 \\ -\Delta_a & -\gamma_a & 0 & 0 & -g & 0 & 0 & 0 \\ 0 & 0 & -\gamma_a & \Delta_a & 0 & g & 0 & 0 \\ 0 & 0 & -\Delta_a & -\gamma_a & -g & 0 & 0 & 0 \\ 0 & g & 0 & g & -\gamma_m & \tilde{\Delta}_m & G_2 & 0 \\ -g & 0 & -g & 0 & -\tilde{\Delta}_m & -\gamma_m & -G_1 & 0 \\ 0 & 0 & 0 & 0 & 0 & 0 & 0 & \omega_b \\ 0 & 0 & 0 & 0 & -G_1 & -G_2 & -\omega_b & -\gamma_b \end{bmatrix}, \tag{6}$$

in which $G_1 = \sqrt{2}\eta\mathrm{Re}(\langle\hat{m}\rangle)$ and $G_2 = \sqrt{2}\eta\mathrm{Im}(\langle\hat{m}\rangle)$ denote effective magnetomechanical coupling. Note that in Eq. (5), we have neglected the second-order fluctuation terms owing them being very small. Furthermore, by performing formal integration on Eq. (5), it can be obtained that

$$\hat{\Phi}(t) = e^{\mathcal{A}t}\hat{\Phi}(0) + \int_0^t e^{\mathcal{A}(t-s)}\hat{n}(s)ds. \tag{7}$$

The prerequisite for studying quantum coherence in this system is that the system is stable. At present, the stability of the cavity-magnomechanical system is determined by the drift matrix $\mathcal{A}$. Based on the Routh–Hurwitz criterion, the specific condition is that the real parts of all eigenvalues of the drift matrix $\mathcal{A}$ (Lyapunov exponents) are less than 0 [118]. Otherwise, the system may exhibit limit cycles or chaotic behavior. Indeed, we can easily determine that if there is an Lyapunov exponents greater than 0, Eq. (7) will definitely diverge over time. Please refer to the Appendix for specific stability conditions. In addition, in the Numerical Results and Discussion section, we also numerically studied the stability parameter regions.

Because the cavity-magnomechanical system being studied shows approximately linear dynamics and is subjected to Gaussian noise, the Gaussian initial state remains invarient throughout the operations. As we know, any Gaussian state can be fully characterized by its first and second moments [10]. Among them, the first moment can be given by steady-state values. The form of the second-order moment, also known as the covariance matrix, under the long-term limit ($t \to \infty$) reads

$$\mathcal{V} = \begin{bmatrix} \mathcal{L}_{\hat{a}_{\updownarrow}} & C_{\hat{a}_{\updownarrow},\hat{a}_{\leftrightarrow}} & C_{\hat{a}_{\updownarrow},m} & C_{\hat{a}_{\updownarrow},b} \\ C_{\hat{a}_{\updownarrow},\hat{a}_{\leftrightarrow}}^{\mathrm{T}} & \mathcal{L}_{\hat{a}_{\leftrightarrow}} & C_{\hat{a}_{\leftrightarrow},m} & C_{\hat{a}_{\leftrightarrow},b} \\ C_{\hat{a}_{\updownarrow},m}^{\mathrm{T}} & C_{\hat{a}_{\leftrightarrow},m}^{\mathrm{T}} & \mathcal{L}_m & C_{m,b} \\ C_{\hat{a}_{\updownarrow},b}^{\mathrm{T}} & C_{\hat{a}_{\leftrightarrow},b}^{\mathrm{T}} & C_{m,b}^{\mathrm{T}} & \mathcal{L}_b \end{bmatrix}, \tag{8}$$

with matrix elements $\mathcal{V}_{\alpha\beta} = \frac{1}{2}[\langle\hat{\Phi}_\alpha(\infty)\hat{\Phi}_\beta(\infty) + \hat{\Phi}_\beta(\infty)\hat{\Phi}_\alpha(\infty)\rangle]$ for $\alpha, \beta = 1 \sim 8$. The covariance matrix $\mathcal{V}$ are real symmetric matrix and positive semidefinite. Each $\mathcal{L}_k$ is a 2×2 matrix, which reflects the local properties of mode k, and each $C_{k,l}$ is also a 2×2 matrix, standing for the quantum correlations between k and l modes ($k, l = \hat{a}_{\updownarrow,\leftrightarrow}, m, b$, and $k \neq l$). The specific form of $\mathcal{V}$ is related to drift matrix $\mathcal{A}$ and diffusion matrix $\mathcal{N}$, i.e., $\mathcal{V} = \int_0^{+\infty} dt(e^{\mathcal{A}t})\mathcal{N}(e^{\mathcal{A}t})^{\mathrm{T}}$ [119]. Here $\mathcal{N} = \mathrm{diag}[\gamma_a(2N_a+1), \gamma_a(2N_a+1), \gamma_a(2N_a+1), \gamma_a(2N_a+1), \gamma_m(2N_m+1), \gamma_m(2N_m+1), 0, \gamma_b(2N_b+1)]$ can be obtained by the noise correlation property, that is, $\langle\hat{n}_\alpha(t_1)\hat{n}_\beta(t_2) + \hat{n}_\beta(t_2)\hat{n}_\alpha(t_1)\rangle/2 = \mathcal{N}_{\alpha\beta}\delta(t_1 - t_2)$. On the other hand, the covariance matrix $\mathcal{V}$ can also be obtained by solving the Lyapunov equation, namely [119],

$$\mathcal{A}\mathcal{V} + \mathcal{V}\mathcal{A}^{\mathrm{T}} = -\mathcal{N}. \tag{9}$$

In the process of quantifying quantum coherence, we obtain the covariance matrix $\mathcal{V}$ by numerically solving Eq. (9).

To facilitate the subsequent discussion of the vector quantum coherence, we define

$$\mathcal{V}_1 = \begin{bmatrix} \mathcal{L}_{\hat{a}_{\updownarrow}} & C_{\hat{a}_{\updownarrow},m} \\ C_{\hat{a}_{\updownarrow},m}^{\mathrm{T}} & \mathcal{L}_m \end{bmatrix}, \quad \mathcal{V}_2 = \begin{bmatrix} \mathcal{L}_{\hat{a}_{\updownarrow}} & C_{\hat{a}_{\updownarrow},b} \\ C_{\hat{a}_{\updownarrow},b}^{\mathrm{T}} & \mathcal{L}_b \end{bmatrix},$$
$$\mathcal{V}_3 = \begin{bmatrix} \mathcal{L}_{\hat{a}_{\leftrightarrow}} & C_{\hat{a}_{\leftrightarrow},m} \\ C_{\hat{a}_{\leftrightarrow},m}^{\mathrm{T}} & \mathcal{L}_m \end{bmatrix}, \quad \mathcal{V}_4 = \begin{bmatrix} \mathcal{L}_{\hat{a}_{\leftrightarrow}} & C_{\hat{a}_{\leftrightarrow},b} \\ C_{\hat{a}_{\leftrightarrow},b}^{\mathrm{T}} & \mathcal{L}_b \end{bmatrix},$$
$$\mathcal{V}_{134} = \begin{bmatrix} \mathcal{L}_{\hat{a}_{\updownarrow}} & C_{\hat{a}_{\updownarrow},m} & C_{\hat{a}_{\updownarrow},b} \\ C_{\hat{a}_{\updownarrow},m}^{\mathrm{T}} & \mathcal{L}_m & C_{m,b} \\ C_{\hat{a}_{\updownarrow},b}^{\mathrm{T}} & C_{m,b}^{\mathrm{T}} & \mathcal{L}_b \end{bmatrix},$$
$$\mathcal{V}_{234} = \begin{bmatrix} \mathcal{L}_{\hat{a}_{\leftrightarrow}} & C_{\hat{a}_{\leftrightarrow},m} & C_{\hat{a}_{\leftrightarrow},b} \\ C_{\hat{a}_{\leftrightarrow},m}^{\mathrm{T}} & \mathcal{L}_m & C_{m,b} \\ C_{\hat{a}_{\leftrightarrow},b}^{\mathrm{T}} & C_{m,b}^{\mathrm{T}} & \mathcal{L}_b \end{bmatrix}. \tag{10}$$

B. Quantifying Gaussian quantum coherence

Suppose a continuous variable Gaussian state with K bosonic modes, its first moment vector and covariance matrix are $\vec{D} = [\vec{d}_1, .., \vec{d}_i, ..\vec{d}_K]$ and V^{tot}, respectively. Here the first moment vector and covariance matrix of the ith mode are $\vec{d}_i$ and V_i. For example, in the current paper, $\vec{d} = [\langle\hat{Q}\rangle, \langle\hat{P}\rangle]$ and $V = \mathcal{L}_m$ for the magnon mode. Accordingly, the quantum

coherence between K bosonic modes can be quantified as [24,25]

$$C_{\rm tot} = C(V^{\rm tot}) = \sum_{i=1}^{K} F(2n_{i,\rm av}+1) - F(\nu_i), \tag{11}$$

with

$$n_{i,\rm av} = \left[{\rm Tr}(V_i) + d_{i,1}^2 + d_{i,2}^2 - 2\right]/4,$$

$$F(x) = \frac{x+1}{2}\log_2\left(\frac{x+1}{2}\right) - \frac{x-1}{2}\log_2\left(\frac{x-1}{2}\right),$$

where Tr refers to performing the trace operation, $F(x)$ describes the entropy of Gaussian systems, and $\nu_i \in \nu$ and ν are the symplectic spectrum of covariance matrix $V^{\rm tot}$, which can be constructed by the eigenspectrum of $|i\tilde{\Omega}V^{\rm tot}|$. Here, $\tilde{\Omega}$ is a $2K\times 2K$ symplectic matrix, which reads [10]

$$\tilde{\Omega} = \sum_{i=1}^{K} \oplus \varpi_i,\ \varpi_i \equiv \begin{bmatrix} 0 & 1 \\ -1 & 0 \end{bmatrix}. \tag{12}$$

Note that Eq. (11) is general and suitable for quantifying quantum coherence of any Gaussian state. Using Eqs. (4) and (8), one can easily obtain the first and second moments of the polarized-driven cavity-magnomechanical system (including any subsystem within it). To explore the polarization-controlled vector quantum coherence, we mark

$$C_{\hat{a}_\updownarrow,m} = C(\mathcal{V}_1), C_{\hat{a}_\updownarrow,b} = C(\mathcal{V}_2), C_{\hat{a}_\leftrightarrow,m} = C(\mathcal{V}_3),$$

$$C_{\hat{a}_\leftrightarrow,b} = C(\mathcal{V}_4), C_{\hat{a}_\updownarrow,m,b} = C(\mathcal{V}_{134}), C_{\hat{a}_\leftrightarrow,m,b} = C(\mathcal{V}_{234}), \tag{13}$$

where $C_{\hat{a}_\updownarrow,m}$, $C_{\hat{a}_\updownarrow,b}$, and $C_{\hat{a}_\updownarrow,m,b}$ are the photon-magnon coherence, the photon-phonon coherence, and the photon-magnon-phonon coherence with respect to the TE mode, respectively. The rest are quantum coherences concerning the TM mode. Physically, the quantum coherence quantifies the degree of superposition of different quantum states.

IV. NUMERICAL RESULTS AND DISCUSSIONS

In this section, we will numerically study the characteristics of quantum coherence,focusing on the polarization-controlled photon-magnon-phonon coherence switch using the intracavity mode. Unless stated otherwise, the simulation parameters used are as follows: $\omega_b/2\pi = 10$ MHz, $\omega_l/2\pi = 10.1$ GHz, $g/2\pi = 3.2$ MHz, $\eta/2\pi = 0.2$ Hz, $T = 10$ mK, $\gamma_a/2\pi = \gamma_m/2\pi = 1$ MHz, $\gamma_b/2\pi = 100$ Hz, $\tilde{\Delta}_m/2\pi = 10$ MHz, $\Delta_a/2\pi = -10$ MHz, $P_l = 2$ mW, $B_0 = 1.3\times10^{-5}$ T, which are experimentally feasible parameters [56–58,73]. We emphasize that the dynamics of the system are described under linearization approximation, so performance parameters beyond this region cannot characterize quantum properties. For this reason, at least one of the microwave driving power P_0 and drive magnetic field B_0 is relatively strong. It is worth mentioning that there is physical reason for choosing $\tilde{\Delta}_m = \omega_b$ [63,66]. In this case, the mechanical mode can be cooled significantly, which is beneficial for the study of quantum coherence. In addition, when $\Delta_a = -\omega_b$, the strong quantum entanglement can be generated [63,100]. Quantum coherence is a necessary condition for quantum entanglement, thereby $\Delta_a = -\omega_b$ is chosen.

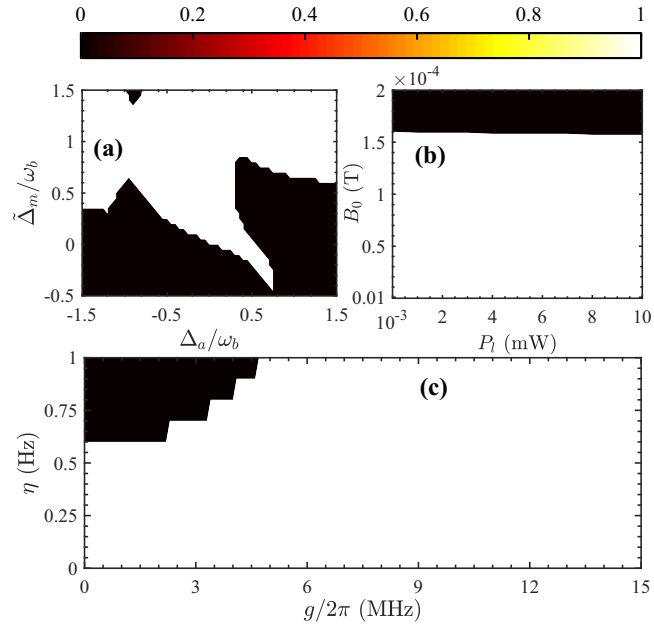

FIG. 2. Stability basins for the steady states of the cavity-magnomechanical system. The evolution of stable (white area) and unstable (black area) areas versus (a) the effective magnon detuning $\tilde{\Delta}_m$ and cavity mode detuning Δ_a, (b) drive magnetic field B_0 and microwave driving power P_l, (c) magnomechanical coupling strength η and microwave-magnon coupling rate g.

A. Stability analysis

A stable system is a prerequisite for studying quantum coherence. Because of the close dependence of stability on the interrelationships and constraints between parameters, it is difficult to determine (see Appendix). To better conduct numerical research on quantum coherence, below we first numerically search for the stable parameter region of the system.

As shown in Fig. 2, the stability of the cavity-magnomechanical system is mapped out by the basins of stability. The steady state of the system is stable for the parameter regions located in the white area, while the black space corresponds to the parameter range leading to unstable fixed points. According to Fig. 2(a), we find that the system in the $\Delta_m < 0$ area is prone to instability and requires an appropriate design of Δ_a to meet stability requirements. When $\Delta_m \geqslant \omega_b$, the stability of the system is relatively easy to satisfy. Figure 2(b) indicates the existence of a very wide area to satisfy the stability of the system. However, when the B_0 is greater than 1.6×10^{-4} T, the stability of the system significantly decreases. Even adjusting power P_l within a large range cannot restore stability to the system. The prominent factor is the large B_0 forcing the YIG sphere to excite a considerable large number of magnons, causing system instability. From Fig. 2(c), we recognize that when $\eta/2\pi < 0.58$ Hz, the cavity-magnomechanical system can easily remain stable without the need for careful design of magnetic-dipole interaction. But in the case of $\eta/2\pi > 0.58$ Hz, to maintain

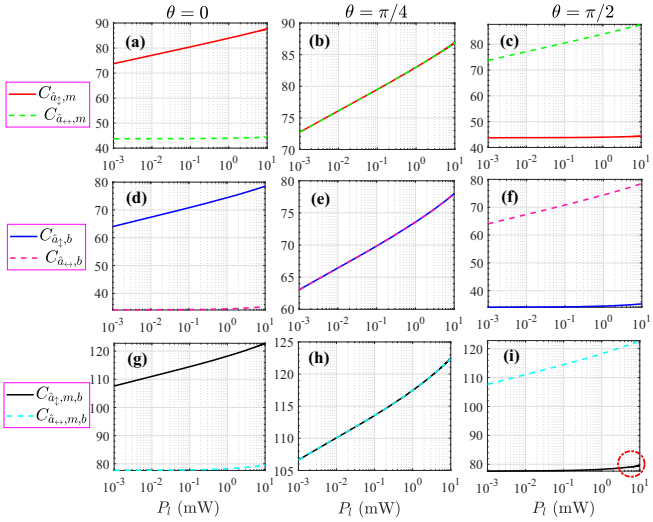

FIG. 3. Three types of quantum coherence versus the microwave driving power P_l (logarithmic coordinate) with the different polarization angle θ for the TE and TM modes, where the column changes in subgraphs correspond to the adjustment of polarization angle, while row changes denote the variation of quantum coherence type.

system stability, the microwave-magnon rate at least should meet $g/2\pi > 4.6$ MHz. Let us recall that combining Fig. 2 with the parameter selection mentioned at the beginning of this section, one can infer that numerical research is indeed conducted under stable conditions.

B. Polarization-controlled vector quantum coherence

In Fig. 3, three types of quantum coherence are shown as functions of the microwave driving power P_l with respect to different polarization angles θ. In real scenarios, the polarization angle can be flexibly adjusted through rotating the orientations of the polarizer. This is essentially controlling the spatial amplitude and phase of the polarized-microwave driving field. We first study the properties of the photon-magnon coherence with respect to the TE and TM modes. In the case of the polarization angle $\theta = 0$, one can see that as the driving power P_l increases, $C_{\hat{a}_\updownarrow,m}$ increases gradually (the increasing trend is almost proportional to $\log P_l$), while $C_{\hat{a}_\leftrightarrow,m}$ remains basically unchanged. Physically, the increase in quantum coherence indicates enhanced quantum interference between modes, which helps establish strong quantum entanglement between modes. Hence, the entanglement between the cavity mode $\hat{a}_\updownarrow$ and magnon mode may increase with the gradual improve in the driving power. Further, the control over the $C_{\hat{a}_\leftrightarrow,m}$ can be achieved through manipulating the polarization angle θ, which we observe in the following content.

When the polarization angle θ changes in the range 0 to $\pi/4$, we see the correlation of m with the vertical and the horizontal cavity mode is the same i.e., $C_{\hat{a}_\updownarrow,m} = C_{\hat{a}_\leftrightarrow,m}$ is always held true and both increase with the increase of P_l. Interestingly, when θ is further increased to $\pi/2$, compared to the situation where $\theta = 0$, $C_{\hat{a}_\updownarrow,m}$ and $C_{\hat{a}_\leftrightarrow,m}$ realize role reversal, namely, $C_{\hat{a}_\leftrightarrow,m}$ gradually increases with the increase of P_l, while $C_{\hat{a}_\updownarrow,m}$ remains unchanged. Further, we can obtain similar results for the photon-phonon coherence $C_{\hat{a}_{\updownarrow(\leftrightarrow)},b}$ and the photon-magnon-phonon $C_{\hat{a}_{\updownarrow(\leftrightarrow)},m,b}$ for the TE and TM modes. The physical mechanism behind this will be analyzed later.

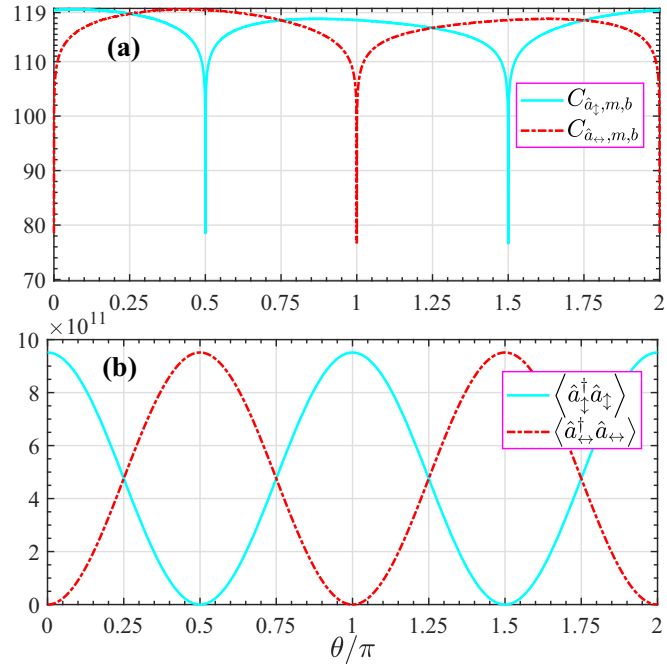

FIG. 4. (a) The photon-magnon-phonon quantum coherence $C_{\hat{a}_{\updownarrow(\leftrightarrow)},m,b}$ as a function of the polarization angle θ for the TE and TM modes. (b) The mean photon numbers $\langle \hat{a}^\dagger_\updownarrow \hat{a}_\updownarrow \rangle$ and $\langle \hat{a}^\dagger_\leftrightarrow \hat{a}_\leftrightarrow \rangle$ with respect to the TE and TM modes versus the the polarization angle θ.

In addition, Fig. 3 shows that $C_{\hat{a}_{\updownarrow(\leftrightarrow)},b} < C_{\hat{a}_{\updownarrow(\leftrightarrow)},m} < C_{\hat{a}_{\updownarrow(\leftrightarrow)},m,b}$ is always held true under the same driving power. This is because the coupling between the orthogonal cavity modes and the magnon is directly caused by the magnetic-dipole interaction, while the interaction between the orthogonal cavity modes and the mechanical mode is indirectly caused via the magnomechanical coupling. Generally speaking, the quantum coherence between two directly interacting modes is greater, so $C_{\hat{a}_{\updownarrow(\leftrightarrow)},b} < C_{\hat{a}_{\updownarrow(\leftrightarrow)},m}$. On the other hand, quantum coherence of single-mode Gaussian states is non-negative, which means that the more the number of modes of the system, the stronger the quantum coherence. This result can also be easily seen through Eq. (11), owing to all summation terms in the equationbeing positive. This is why the photon-magnon-phonon coherence $C_{\hat{a}_{\updownarrow(\leftrightarrow)},m,b}$ is greater than $C_{\hat{a}_{\updownarrow(\leftrightarrow)},m}$and $C_{\hat{a}_{\updownarrow(\leftrightarrow)},b}$. In the subsequent discussion, we focus on the characteristics of the photon-magnon-phonon quantum coherence $C_{\hat{a}_{\updownarrow(\leftrightarrow)},m,b}$ with respect to the TE and TM modes.

Presented in Fig. 4(a) is the variation of $C_{\hat{a}_\updownarrow,m,b}$ and $C_{\hat{a}_\leftrightarrow,m,b}$ with the polarization angle θ in a period of 0 to 2π, manifesting that as the polarization angle changes, $C_{\hat{a}_\updownarrow,m,b}$ and $C_{\hat{a}_\leftrightarrow,m,b}$ always exhibit a complementary distribution. This means that an adjustable photon-magnon-phonon quantum coherence conversion between the orthogonal cavity modes TE and TM modes can be implemented through a coherent polarization control. Physically, this is because, in the polarized-microwave-driven cavity-magnomechanical system, the steady-state average photon number of the

orthogonal cavity modes closely relies on the spatial distribution of the polarized-microwave driving field [as shown in Fig. 4(b)]. As a consequence, the effective coupling between orthogonal cavity modes and associated magnon as well as phonon modes also depends on θ. Particularly, for a certain polarization angle, when one of the orthogonal cavity modes has a strong effective coupling with the magnon and phonon modes, the effective coupling between the other orthogonal cavity mode and the magnon as well as phonon modes will be weaker. Indeed, by comparing the two subgraphs, one can clearly see that the valley-peak positions of the photon-magnon-phonon coherence and that of its average photon number for TE (TM) modes are completely consistent, indicating that the mean photon number of orthogonal cavity modes directly determines the photon-magnon-phonon coherence. In practical applications, the ability to achieve an adjustable quantum coherence conversion between the orthogonal cavity modes TE and TM modes would provide another degree of freedom for quantum communication based on cavity-magnomechanical systems. On the other hand, the coherent conversion of $C_{\hat{a}_\updownarrow,m,b}$ and $C_{\hat{a}_\leftrightarrow,m,b}$ also indicates that the quantum superposition degree between magnons and phonons and the two orthogonal cavity modes varies in a similar way with the polarization angle.

Similarly, at an appropriate polarization angle, increasing the microwave driving power will lead to an increase in the average photon number, thereby increasing quantum coherence (see Fig. 3). Note that there are also some special polarization angles ($\theta = \pi k/2, k \in \mathbb{Z}$) where at least one mode's mean photon number (TE or TM) is insensitive to microwave driving power. This corresponds to the situation where quantum coherence remains basically unchanged as P_l increases (see Fig. 3). It is worth mentioning that even though the average photon number of a certain orthogonal cavity mode is not sensitive to P_l. However, when P_l is large, the quantum coherence related to this mode can still be affected due to indirect interactions between subsystems, as shown in the red circle in the bottom right corner of Fig. 3(i).

In Fig. 5, we show $C_{\hat{a}_\updownarrow,m,b}$ and $C_{\hat{a}_\leftrightarrow,m,b}$ as functions of the driving magnetic field B_0 and the polarization angle θ. It displays that the $C_{\hat{a}_\updownarrow,m,b}$ and $C_{\hat{a}_\leftrightarrow,m,b}$ are increased with the increase of B_0. The underlying physics can be understood as follows. Increasing B_0 will cause a stronger coupling rate Ω_l, leading to a significant increase in the mean magnon number, ultimately enhancing the photon-magnon-phonon quantum coherence. The significance of this result is that increasing the quantum coherence between modes may contribute to the measurement of magnetic fields and help us achieve high sensitivity magnetometers [3].

Considering the close relationship between the mean magnon number and the driving magnetic field B_0 may affect the validity of the model and linearization approximation. To address readers' concerns, we now discuss this issue. When $B_0 = 1\times10^{-6}$ T, this corresponds to a weak driving magnetic field. However, note that we also applied a relatively strong polarized-microwave drive to the 3D microwave cavity, and there is the state-swap interaction between the orthogonal cavity modes and the magnon. Thus, the steady-state mean magnon number can still reach up to $\langle\hat{m}^\dagger\hat{m}\rangle \simeq 2.49\times10^{11}$, so the linearization approximation

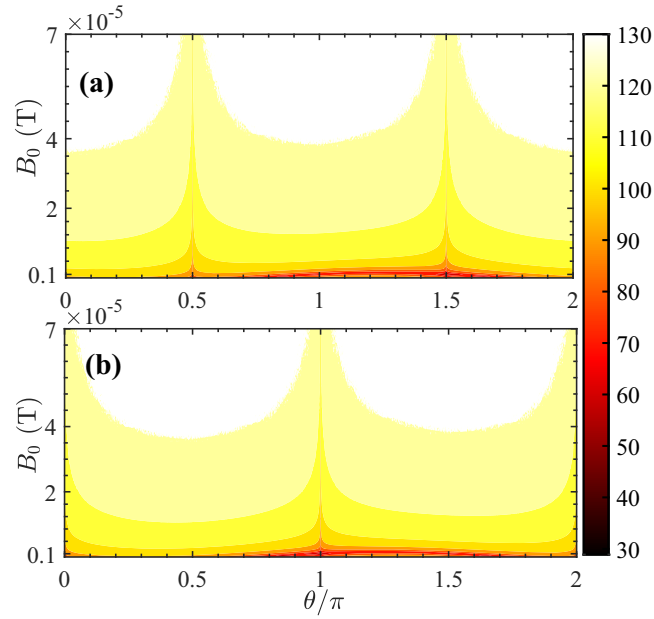

FIG. 5. Density plot of the photon-magnon-phonon coherence (a) $C_{\hat{a}_\updownarrow,m,b}$ and (b) $C_{\hat{a}_\leftrightarrow,m,b}$ with respect to the TE and TM modes versus the drive magnetic field B_0 and the polarization angle θ.

holds. In addition, in the case of $B_0 = 7\times10^{-5}$ T, the steady-state mean magnon number $\langle\hat{m}^\dagger\hat{m}\rangle \simeq 2.96\times10^{14} \ll 2NS = 1.75\times10^{17}$ holds, where $S = 5/2$ denotes the spin quantum number of the ground state Fe^{3+} ion in the YIG sphere. This means that the low-lying excitations assumption made using Holstein-Primakoff transformation in deriving the Hamiltonian $\hat{H}$ has not been violated. On the other hand, due to the strong polarized-microwave driving of the orthogonal cavity modes, even under weak driving magnetic fields, it may significantly reveal magnon Kerr effect. Fortunately, at the driving magnetic field $B_0 = 1\times10^{-6}$ T and $B_0 = 7\times10^{-5}$ T, $\mathcal{K}|\langle\hat{m}\rangle|^3/\Omega_l$ is approximately $2.72\times10^{-4} \ll 1$ and $0.12 \ll 1$, respectively, where $\mathcal{K} \simeq 2\pi\times6.4$ nHz denotes the Kerr coefficient for a 250-μm-diameter YIG sphere. Accordingly, the Kerr nonlinearity effect can also be safely neglected in the current model. Particularly, based on the formula $B_0 = \frac{1}{R}\sqrt{\frac{2P_B\mu_0}{\pi c}}$ [63,66], one can infer the power (P_B) of the microwave source driving YIG sphere. Here R (125 μm), c, and μ_0 are the radius of the YIG sphere, the velocity of electromagnetic wave in vacuum, and the vacuum magnetic permeability, respectively.

It is practically meaningful to investigate the influence of the ambient temperature on quantum coherence. In Fig. 6, the photon-magnon-phonon coherence $C_{\hat{a}_\updownarrow,m,b}$ and $C_{\hat{a}_\leftrightarrow,m,b}$ are plotted as a function of the temperature T and the polarization angle θ. Consistent with our expectations, with the increase of temperature, both $C_{\hat{a}_\updownarrow,m,b}$ and $C_{\hat{a}_\leftrightarrow,m,b}$ decrease at the same time. This can be understood as follows. When the ambient temperature is raised, the equilibrium mean thermal mode (photon, magnon, and phonon) numbers in the cavity-magnomechanical system increase, i.e., an increase in incoherent modes. At higher temperature, the equilibrium mean thermal mode numbers are approximately proportional to $k_BT/\hbar\omega_k$ ($k = a, m, b$). As such, the decoherence effect of

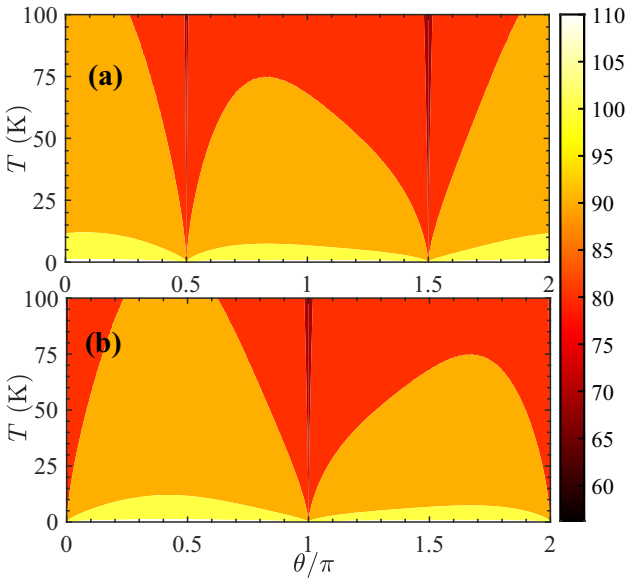

FIG. 6. Density plot of the photon-magnon-phonon coherence (a) $C_{\hat{a}_\updownarrow,m,b}$ and (b) $C_{\hat{a}_\leftrightarrow,m,b}$ versus the ambient temperature T and the polarization angle θ.

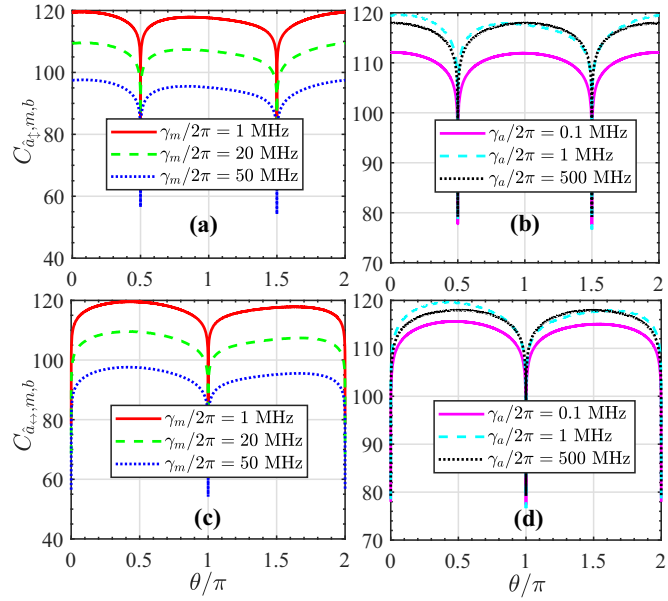

FIG. 7. Plot of the photon-magnon-phonon coherence with respect to the TE and TM modes versus the polarization angle θ with the different magnon damping γ_m (a), (c) and cavity mode decay rate γ_a (b), (d).

the orthogonal cavity modes, magnon and phonon, become stronger, leading to the photon-magnon-phonon coherence $C_{\hat{a}_\updownarrow,m,b}$ and $C_{\hat{a}_\leftrightarrow,m,b}$ being reduced. Importantly, one finds that the photon-magnon-phonon coherence can last to a very high temperature. Even when the ambient temperature reaches $T =$ 100 K, $C_{\hat{a}_\updownarrow,m,b}$ and $C_{\hat{a}_\leftrightarrow,m,b}$ still remain at a relatively high value, indicating strong robustness to the ambient temperature. Particularly, the quantum coherence that can withstand high temperatures is a prerequisite for achieving joint manipulation of quantum states in practice. This is in sharp contrast to the photon-magnon-phonon entanglement, since the entanglement can only last until about 0.2 K [63].

Besides the ambient temperature, it is also very important to explore the influence of damping channels on quantum resources. In Fig. 7, we explore the dependence of photon-magnon-phonon coherence $C_{\hat{a}_\updownarrow,m,b}$ and $C_{\hat{a}_\leftrightarrow,m,b}$ on the magnon damping γ_m and the cavity mode decay rate γ_a. It can be found from Figs. 7(a) and 7(c) that, with the increase of γ_m, both $C_{\hat{a}_\updownarrow,m,b}$ and $C_{\hat{a}_\leftrightarrow,m,b}$ decrease at the same time. The reason is that when γ_m is increased, the mean magnon number in the cavity-magnomechanical system decreases, which indirectly leads to a decrease in the average number of orthogonal cavity modes and phonon mode [see Eq. (4)]. In addition, the diffusion matrix $\mathcal{N}$is also amplified, which is a noncoherent operation. The two effects together result in a decrease in $C_{\hat{a}_\updownarrow,m,b}$ and $C_{\hat{a}_\leftrightarrow,m,b}$. It is important to note that even in high-decay rate areas, $C_{\hat{a}_\updownarrow,m,b}$ and $C_{\hat{a}_\leftrightarrow,m,b}$ still present a complementary distribution with changes in the polarization angle.

However, it is surprising that increasing γ_a not only does not reduce $C_{\hat{a}_\updownarrow,m,b}$ and $C_{\hat{a}_\leftrightarrow,m,b}$, but also significantly increases quantum coherence, as shown in Figs. 7(b) and 7(d) (see the pink solid line and the sky blue dashed line, respectively). Particularly, when γ_a increases from $2\pi\times1$ MHz to $2\pi\times500$ MHz, $C_{\hat{a}_\updownarrow,m,b}$ and $C_{\hat{a}_\leftrightarrow,m,b}$ only show a very slight decrease (even remaining unchanged at certain polarization angles). Physically, this is because the cavity mode decay rate generally destroys cavity modes and then suppresses the quantum coherence. On the other hand, based on the relation $E_l = \sqrt{2\gamma_a P_l/\omega_l}$, the cavity mode decay rate is also helpful to directly establish the orthogonal cavity mode. Specifically, in the case of small γ_a, the latter plays a main role, yielding the increase of $C_{\hat{a}_\updownarrow,m,b}$ and $C_{\hat{a}_\leftrightarrow,m,b}$. When γ_a is large, the former plays a pivotal role, leading to a decrease in $C_{\hat{a}_\updownarrow,m,b}$ and $C_{\hat{a}_\leftrightarrow,m,b}$. This means that there is a critical γ_a^c that can give the maximum photon-magnon-phonon coherence. In addition, when the two effects of γ_a reach equilibrium, $C_{\hat{a}_\updownarrow,m,b}$ and $C_{\hat{a}_\leftrightarrow,m,b}$ tend to saturate. In this scenario, if we continue to increase γ_a, there will be no noticeable change in the photon-magnon-phonon coherence. Comparing the black and sky blue curves in Figs. 7(b) and 7(d) are sufficient to justify this. Particularly, the coherent conversion between $C_{\hat{a}_\updownarrow,m,b}$ and $C_{\hat{a}_\leftrightarrow,m,b}$ is not disrupted by the dissipative channels. This is because the dissipative channels will not change the ratio of the number of photons in the two orthogonal cavity modes. This ratio only depends on the polarization angle θ. This means that the coherent conversion of the photon-magnon-phonon quantum coherence achieved in our work is noise immune and can be practically applied in vector quantum communication and quantum network tasks.

On the other hand, it is also interesting to mention that $C_{\hat{a}_\updownarrow,m,b}$ and $C_{\hat{a}_\leftrightarrow,m,b}$ are very robust to the mechanical decay rate γ_b. Even if we change γ_b from $2\pi\times10^2$ Hz to $2\pi\times10^6$ Hz, there is no noticeable change in $C_{\hat{a}_\updownarrow,m,b}$ and $C_{\hat{a}_\leftrightarrow,m,b}$. Here we attempt to provide a physical explanation for this phenomenon. Based on Eq. (4), we note that γ_b does not reduce the mean phonon number, and only one term in the diffusion matrix $\mathcal{N}$contains γ_b. These are the main differences between γ_b and γ_a (γ_m), so the impact of γ_b on $C_{\hat{a}_\updownarrow,m,b}$ and $C_{\hat{a}_\leftrightarrow,m,b}$ is not significant.

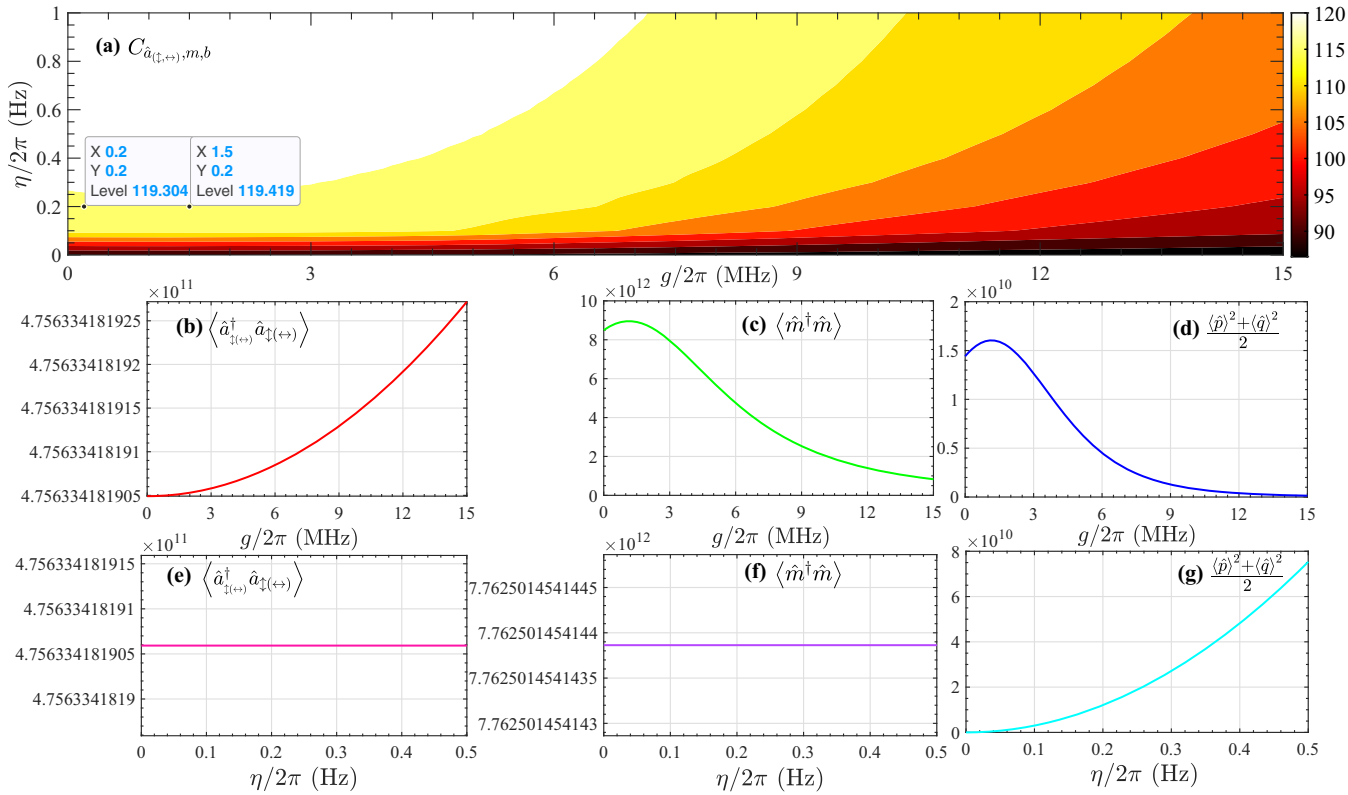

FIG. 8. (a) Density plot of the photon-magnon-phonon coherence $C_{\hat{a}_\updownarrow,m,b}$ and $C_{\hat{a}_\leftrightarrow,m,b}$ versus the microwave-magnon coupling strength g and the magnomechanical coupling rate η. The mean number for various modes (photon, magnon, and phonon) as a function of g (b)–(d) and η (e)–(f). Here we set the polarization angle $\theta = \pi/4$, indicating that $C_{\hat{a}_\updownarrow,m,b} \equiv C_{\hat{a}_\leftrightarrow,m,b}$.

The dependence of the photon-magnon-phonon coherence $C_{\hat{a}_{\updownarrow(\leftrightarrow)},m,b}$ on the microwave-magnon coupling strength g and the magnomechanical coupling rate η is shown in Fig. 8(a), manifesting that the largest $C_{\hat{a}_{\updownarrow(\leftrightarrow)},m,b}$ is achieved at the left top corner. Specifically, with fixed magnomechanical coupling rate η, we find that $C_{\hat{a}_{\updownarrow(\leftrightarrow)},m,b}$ first increases slightly (see two marker points) with the increase of g and then undergoes a decreasing trend. The physical reason behind this is that although increasing g can enhance the swap-interaction between photons and magnons, it also leads to the sharp decrease of mean magnon and phonon numbers, as shown in Figs. 8(c) and 8(d). Note also that mean photon number is only slightly increased by enhancing g, as shown in Fig. 8(b). Consequently, when g is large, the photon-magnon-phonon coherences with respect to the TE and TM mode are suppressed.

When fixing the cavity-magnon coupling rate g, and increasing η, $C_{\hat{a}_{\updownarrow(\leftrightarrow)},m,b}$ is gradually increased. Physically, η corresponds to the magnomechanical coupling, which is a radiation pressurelike coupling and beneficial for establishing the entanglement between magnon and phonon modes. Therefore, generally speaking, the magnomechanical coupling can also promote the photon-magnon-phonon coherence. On the other hand, we can see that although the mean phonon and magnon numbers do not show significant changes with the enhancement of η [see Figs. 8(e) and 8(f)], the mean phonon number increases [see Fig. 8(g)]. This is also another reason why increasing η can lead to an increase in $C_{\hat{a}_{\updownarrow(\leftrightarrow)},m,b}$.

V. EXPERIMENTAL FEASIBILITY AND DETECTION OF THE POLARIZATION-CONTROLLED QUANTUM COHERENCE

From a practical perspective, it is necessary to discuss the experimental feasibility and detection of the photon-magnon-phonon coherence in the polarized-microwave-driven cavity-magnomechanical system.

A. Experimental feasibility

First, we would like to point out that the technology to manufacture optical polarizers is very mature, and utilizing it to generate polarized microwaves has been widely used in optical engineering [42]. In addition, the optical polarizer has excellent integration performance [53,54,120], allowing it to be well integrated with the cavity-magnomechanical system. Second, the cavity-magnomechanical system has been experimentally implemented to verify some interesting quantum effects, including dynamical backaction effects [121], magnon-spring effect [56], optical response [58], and more. This means that experimental physicists possess the ability to detect quantum effects in a cavity-magnomechanical system. Third, the parameters used in the numerical simulation process are experimentally feasible. Moreover, the photon-magnon-phonon coherences for the TE and TM modes show strong robustness to the environment temperature and mechanical damping. More importantly, some works have reported experimental demonstrations of continuous variable quantum coherence in Gaussian states [38,39]. On the basis of the above contents,

we believe that the polarization controlled quantum coherence in cavity-magnomechanical systems is expected to be realized under the current experimental technology.

B. Strategy for detecting the quantum coherence

Presently, the coherence studied belongs to continuous variable quantum coherence (or Gaussian quantum coherence). It is clear that the preferred methods for detecting this polarization-controlled quantum coherence are the homodyne or heterodyne detection schemes, which is similar to experimentally detecting the optomechanical entanglement [119]. Specifically, the quantum coherence is mainly included in the covariance matrix of the cavity-magnomechanical system. The reconstruction of the covariance matrix is closely related to the quadrature operators of the system. First, we can directly read quadratures of orthogonal cavity modes by the homodyne or heterodyne method. However, measuring the magnon and phonon modes are less straightforward. An effective method is coupling the YIG sphere to the auxiliary optical cavity, which is driven by a weak red-detuned laser [105]. In this scenario, the information regarding the magnon and phonon modes can be indirectly obtained from the output of the readout field. Finally, the photon-magnon-phonon coherence in the polarized-microwave-driven cavity-magnomechanical system could be detected by measuring the reconstructed covariance matrix under a proper readout choice via a spectral filter. It is necessary to mention that the function of spectral filter is to extract a set of independent output quadratures from different frequencies or time intervals of continuous output fields. In the above process, we need to utilize the standard input-output relations for obtaining the output quadratures [115]. Particularly, a suitable choice for the causal filter function is [122]

$$\varphi(t) = \frac{\vartheta(t) - \vartheta(t-s)}{\sqrt{s}} e^{-i\Omega t}, \tag{14}$$

with

$$\vartheta(t) = \begin{cases} 0, & t < 0 \\ 1, & t \geqslant 0. \end{cases}$$

Here $\vartheta(t)$ is the Heaviside step function; Ω and s^{-1} denotes the central frequency and the bandwidth of the causal filter, respectively. Note also that to obtain the covariance matrix, we must take the time traces, multiply them, and then take the average of various quadrature products.

VI. DISCUSSIONS AND CONCLUSIONS

A. Discussions

Finally, let's discuss the physical insight into this quantum coherence and its possible connection with previous multipoint correlation functions. Coherence has always been at the core of the development of quantum optics and was usually studied from the perspective of phase space distributions and multipoint correlation functions [6,7]. However, in our paper, the quantization of Gaussian quantum coherence is based on relative entropy [24]. There are recent developments about quantitative characterization of coherence. Physically, the relative entropy describes the distance measures between different modes. From this perspective, our calculation results [see Eq. (13)] reflect the degree of correlation between photon, magnon, and phonon modes. In other words, the Gaussian quantum coherence between these modes quantifies the degree of superposition of quantum states of different modes. Mathematically, it manifests as the density matrix of the cavity-magnomechanical system being nondiagonal. In addition, the photon-magnon-phonon/photon-magnon coherence also embodies the essence of the quantum interference and multipartite entanglement between these modes. In this sense, our calculation results may quantitatively describe the degree of quantization of this continuous variable cavity-magnomechanical system [6,7]. From a practical point of view, quantum coherence is the key ingredient that drives quantum technologies, so the precise quantification of photon-magnon/photon-magnon-phonon coherence has application in the fields of continuous variable quantum information and quantum communication. In this sense, our results capture the resource characteristics of physical parameters of a cavity-magnomechanical system in a mathematically rigorous way. Moreover, the photon-magnon-phonon/photon-magnon coherence is also a prerequisite for achieving joint quantum operation of these mode states [6,7]. More importantly, our study achieved coherence conversion of the photon-magnon-phonon coherence through an optical polarizer, improving the flexibility of quantum coherence control in practice. This is another degree of freedom for controlling quantum coherence.

Meanwhile, we believe that the method of relative entropy may be equivalent to phase-space distributions and multipoint correlation functions. For example, there *may be* a multipoint quantum correlation function $g_{\mathrm{pho,mag}} \propto \langle \hat{a}_j^{\dagger} \hat{a}_j \hat{m}^{\dagger} \hat{m} \rangle$ (where $j = \updownarrow, \leftrightarrow$; note that its specific form remains an open question) to represent the quantum coherence between photon and magnon. This result should be equivalent to our calculation result. In this sense, we can also use methods similar to the Hanbury Brown-Twiss experiment [18] to measure Gaussian quantum coherence, but, currently, Gaussian quantum coherence between modes is only measured by measuring the first-order moment and covariance matrix [38]. As a result, a future research direction may be to establish a bridge between the current method for quantifying Gaussian quantum coherence and a previous method for multipoint correlation functions.

B. Conclusions

In summary, we have theoretically investigated the vector photon-magnon-phonon coherence in a polarized-microwave-driven cavity-magnomechanical system. The results indicated that, by modulating the polarization angle of optical polarizer, we can achieve coherent conversion between the two types of photon-magnon-phonon coherence with respect to the TE and TM modes. Such an ability coherently switching the macroscopic quantum coherence is expected to offer unprecedented opportunities for quantum communication and quantum information processing based on continuous variables. In addition, we also revealed the impact of other physical factors on the vector photon-magnon-phonon coherence and delved into the underlying physical mechanisms. Not limited to linear polarized microwaves and the vector

quantum coherence, we can also introduce other generalized vector fields (e.g., cylindrical vector beam or full Poincaré beam) into the cavity-magnomechanical system in the future to investigate other interesting quantum effects. Our study has laid the groundwork for further exploration of vector cavity-magnomechanical systems.

ACKNOWLEDGMENTS

J.-X.P. thanks Professor Jianwei Xu for his insightful discussions. This work was supported by the National Science Foundation (NSF) of China (Grant No. 12105047), Guangdong Basic and Applied Basic Research Foundation (Grant No. 2022A1515010446). M.A. has been supported by the Khalifa University of Science and Technology under Award No. FSU-2023-014. A.K. acknowledges support from the Polish National Science Center under Grant Agreement No. 2019/33/B/ST6/02011.

APPENDIX: STABILITY CONDITIONS OF SYSTEM

The drift matrix $\mathcal{A}$ of the known cavity-magnomechanical system reads

$$\mathcal{A}=\begin{bmatrix} -\gamma_a & \Delta_a & 0 & 0 & 0 & g & 0 & 0 \\ -\Delta_a & -\gamma_a & 0 & 0 & -g & 0 & 0 & 0 \\ 0 & 0 & -\gamma_a & \Delta_a & 0 & g & 0 & 0 \\ 0 & 0 & -\Delta_a & -\gamma_a & -g & 0 & 0 & 0 \\ 0 & g & 0 & g & -\gamma_m & \tilde{\Delta}_m & G_2 & 0 \\ -g & 0 & -g & 0 & -\tilde{\Delta}_m & -\gamma_m & -G_1 & 0 \\ 0 & 0 & 0 & 0 & 0 & 0 & 0 & \omega_b \\ 0 & 0 & 0 & 0 & -G_1 & -G_2 & -\omega_b & -\gamma_b \end{bmatrix}. \tag{A1}$$

To obtain the stability conditions, we need to apply the Routh-Hurwitz criterion [118]. The subsequent steps outline the process for identifying the stability parameters of the cavity-magnomechanical system. Using the drift matrix, we first construct the eigenequation of $\mathcal{A}$, which satisfies

$$|\mathcal{A}-\lambda\mathbb{1}_8|=0, \tag{A2}$$

where $\mathbb{1}_8$ is the 8×8 identity matrix and λ is a scalar. Solving Eq. (A2), yielding the characteristic equation

$$A\lambda^8+B\lambda^7+C\lambda^6+D\lambda^5+E\lambda^4+F\lambda^3+G\lambda^2+K\lambda+L=0, \tag{A3}$$

where

$$\begin{aligned}
&A=1, B=4\gamma_a+\gamma_b, C=4g^2+6\gamma_a^2+4\gamma_a\gamma_b-\gamma_m^2+\tilde{\Delta}_m^2+\omega_b\omega_m,\\
&D=12g^2\gamma_a+4\gamma_a^3+4g^2\gamma_b+6\gamma_a^2\gamma_b-4\gamma_a\gamma_m^2-\gamma_b\gamma_m^2+4\gamma_a\tilde{\Delta}_m^2+\gamma_b\tilde{\Delta}_m^2+4\gamma_a\omega_b,\\
&E=4g^4+12g^2\gamma_a^2+\gamma_a^4+12g^2\gamma_a\gamma_b+4\gamma_a^3\gamma_b-6\gamma_a^2\gamma_m^2-4\gamma_a\gamma_b\gamma_m^2-\Delta_a^4-2g^2\Delta_a\tilde{\Delta}_m,\\
&\quad+6\gamma_a^2\tilde{\Delta}_m^2+4\gamma_a\gamma_b\tilde{\Delta}_m^2+2G_1G_2\gamma_m\omega_b-G_1^2\tilde{\Delta}_m\omega_b-G_2^2\tilde{\Delta}_m\omega_b+4g^2\omega_b\omega_m+6\gamma_a^2\omega_b-\gamma_m^2\omega_b+\tilde{\Delta}_m^2\omega_b,\\
&F=8g^4\gamma_a+4g^2\gamma_a^3+4g^4\gamma_b+12g^2\gamma_a^2\gamma_b+\gamma_a^4\gamma_b-4\gamma_a^3\gamma_m^2-6\gamma_a^2\gamma_b\gamma_m^2-\Delta_a^4-4g^2\gamma_a\Delta_a\delta_m-2g^2\gamma_b\Delta_a\tilde{\Delta}_m\\
&\quad+4\gamma_a^3+6\gamma_a^2\gamma_b\Delta_m^2+8G_1G_2\gamma_a\gamma_m\omega_b-4G_1^2\gamma_a\tilde{\Delta}_m\omega_b-4G_2^2\gamma_a\tilde{\Delta}_m\omega_b+12g^2\gamma_a\omega_b+4\gamma_a^3\omega_b-4\gamma_a\gamma_m^2\omega_b+4\gamma_a\tilde{\Delta}_m^2\omega_b,\\
&G=4g^4\gamma_a^2+8g^4\gamma_a\gamma_b+4g^2\gamma_a^3\gamma_b-\gamma_a^4\gamma_m^2-4\gamma_a^3\gamma_b\gamma_m^2+\gamma_m^2\delta_a^4-2g^2\gamma_a^2\Delta_a\tilde{\Delta}_m-4g^2\gamma_a\gamma_b\Delta_a\tilde{\Delta}_m+2g^2\Delta_a^3\tilde{\Delta}_m\\
&\quad+\gamma_a^4\tilde{\Delta}_m^2+4\gamma_a^3\gamma_b\tilde{\Delta}_m^2-\Delta_a^4\tilde{\Delta}_m^2+12G_1G_2\gamma_a^2\gamma_m\omega_b+2g^2G_1^2\Delta_a\omega_b-6G_1^2\gamma_a^2\Delta_m\omega_b-6G_2^2\gamma_a^2\tilde{\Delta}_m\omega_b\\
&\quad+4g^4\omega_b+12g^2\gamma_a^2\omega_b+\gamma_a^4\omega_b-6\gamma_a^2\gamma_m^2\omega_b-\Delta_a^4\omega_b-2g^2\Delta_a\tilde{\Delta}_m\omega_b\tilde{\Delta}_m+6\gamma_a^2\tilde{\Delta}_m^2\omega_b,\\
&K=4g^4\gamma_a^2\gamma_b-\gamma_a^4\gamma_b\gamma_m^2+\gamma_b\gamma_m^2\Delta_a^4-2g^2\gamma_a^2\gamma_b\Delta_a\tilde{\Delta}_m+2g^2\gamma_b\Delta_a^3\tilde{\Delta}_m+\gamma_a^4\gamma_b\tilde{\Delta}_m^2-\gamma_b\Delta_a^4\tilde{\Delta}_m^2+8G_1G_2\gamma_a^3\gamma_m\omega_b\\
&\quad+4g^2G_1^2\gamma_a\Delta_a\omega_b-4G_1^2\gamma_a^3\tilde{\Delta}_m\omega_b-4G_2^2\gamma_a^3\tilde{\Delta}_m\omega_b+8g^4\gamma_a\omega_b+4g^2\gamma_a^3\omega_b-4\gamma_a^3\gamma_m^2\omega_b,-4g^2\gamma_a\Delta_a\tilde{\Delta}_m\omega_b+4\gamma_a^3\tilde{\Delta}_m^2\omega_b,\\
&L=2G_1G_2\gamma_a^4\gamma_m\omega_b+2g^2G_1^2\gamma_a^2\Delta_a\omega_b-2g^2G_2^2\Delta_a^3\omega_b-2G_1G_2\gamma_m\Delta_a^4\omega_b-G_1^2\gamma_a^4\tilde{\Delta}_m\omega_b-G_2^2\gamma_a^4\tilde{\Delta}_m\omega_b\\
&\quad+G_1^2\Delta_a^4\tilde{\Delta}_m\omega_b+G_2^2\Delta_a^4\tilde{\Delta}_m\omega_b+4g^4\gamma_a^2\omega_b-\gamma_a^4\gamma_m^2\omega_b+\omega_b-2g^2\gamma_a^2\Delta_a\tilde{\Delta}_m\omega_b+2g^2\Delta_a^3\tilde{\Delta}_m\omega_b+\tilde{\Delta}_m^2\omega_b-\Delta_a^4\tilde{\Delta}_m^2\omega_b.
\end{aligned}$$

Based on these coefficients, we can construct the stability Table I. According to the Routh-Hurwitz criterion [118], the necessary and sufficient condition for stability of the system is to make sure that each term in Col_1 (namely, A, B, T_1, U_1, V_1, W_1, X_1, Y_1) is positive when $A>0$. To ensure positivity in each term of Col_1, the parameters of the

TABLE I. In the table, $T_1 = (BC - AD)/B$, $T_2 = (BE - AF)/B$, and the other T_s can be evaluated similarly. Meanwhile, $U_1 = (T_1D - T_2B)/T_1$, $U_2 = (T_1F - T_3B)/T_1$, and, in a similar manner, $V_1 = (U_1T_2 - U_2T_1)/U_1$, $W_1 = (V_1U_2 - V_2U_1)/V_1$, $X_1 = (W_1V_2 - V_1W_2)/W_1$ and finally $Y_1 = (X_1W_2 - W_1X_2)/W_1$. It should be noted that the empty cells denote null value.

	Col_1	Col_2	Col_3	Col_4	Col_5
S^8	A	C	E	G	L
S^7	B	D	F	K	
S^6	T_1	T_2	T_3	T_4	
S^5	U_1	U_2	U_3		
S^4	V_1	V_2	V_3		
S^3	W_1	W_2			
S^2	X_1	X_2			
S	Y_1				
S^0					

cavity-magnomechanical system must comply to the specific constraints, i.e.,

$$c_1 = 4\gamma_a + \gamma_b > 0, \tag{A4}$$

$$c_2 = \left(G_1^2 + G_2^2\right)\tilde{\Delta}_m - 2G_1G_2\gamma_m > 0, \tag{A5}$$

$$c_3 = \tilde{\Delta}_m(\Delta_a + \tilde{\Delta}_m) - \gamma_m^2 > 0, \tag{A6}$$

$$c_4 = 2g^4 + g^2\gamma_b^2 + \Delta_a^2 + g^2c_3 + \omega_bc_2 - g^2\gamma_m^2 - 2g^2\omega_b\omega_m > 0, \tag{A7}$$

$$c_5 = g^4 + \Delta_a^4 + g^2c_3 + \gamma_b(g^2 + \omega_m\omega_b) > 0, \tag{A8}$$

$$c_6 = 15g^2 + 5\gamma_b^2 + 6\omega_b\omega_m > 0, \tag{A9}$$

$$c_7 = 64\gamma_a^6 + 116\gamma_a^5\gamma_b + 80\gamma_a^4\left(g^2 + \gamma_b^2\right) + \gamma_b^2c_2\omega_b + 4\gamma_a^3\gamma_bc_6 + 4\gamma_a\gamma_bc_4 + 16\gamma_a^2c_5 - c_1 > 0, \tag{A10}$$

$$4\gamma_a\left(g^2 + 5\gamma_a^2 + 4\gamma_a\gamma_b + \gamma_b^2\right) + \gamma_b\omega_b\omega_m > c_1, \tag{A11}$$

$$k_{13}\gamma_a^4\gamma_b + 2k_{15}\gamma_a^2\gamma_b + 4k_{12}\gamma_a^5 + 4k_{16}\gamma_a^3 + 4k_{14}\gamma_a + k_{11}\gamma_b\omega_b + c_7k_{10}c_1^{-2} > k_5k_6c_1^{-1}, \tag{A12}$$

where

$$k_1 = g^2 - \gamma_m^2 + \tilde{\Delta}_m^2, \quad k_2 = 2k_4 - \Delta_a^4, \quad k_3 = 6g^2 + k_1,$$
$$k_4 = 2g^4 - g^2\Delta_a\tilde{\Delta}_m,$$
$$k_5 = 4\gamma_a\left(4\gamma_a\gamma_b + 5\gamma_a^2 + \gamma_b^2 + g^2\right) + \gamma_b\omega_b\omega_m,$$
$$k_6 = \gamma_a^4\gamma_b + 12k_1\gamma_a^2\gamma_b + 4\gamma_a^3(\omega_b\omega_m + k_1) + 12k_1\gamma_a\omega_b\omega_m - 4c_2\gamma_a + 4k_4\gamma_a + k_2\gamma_b,$$
$$k_7 = \gamma_b^2 + 5\omega_b\omega_m + k_3, \quad k_8 = 3\omega_b\omega_m + 24g^2 + 8\tilde{\Delta}_m^2,$$
$$k_9 = g^2\omega_b\omega_m + 3k_1\gamma_b^2 + k_4,$$
$$k_{10} = 16\gamma_a^4\gamma_b + 2k_8\gamma_a^2\gamma_b - 16\gamma_a^2\gamma_b\gamma_m^2 - 4\gamma_a\Delta_a^4 + 4\gamma_a^5 + 4\gamma_a + 4k_7\gamma_a^3 - c_2\gamma_b\omega_b, + \gamma_b\omega_b\left(4g^2 + \delta_m^2\right) - \gamma_b\omega_b\gamma_m^2\omega_m,$$
$$k_{11} = 2g^2G_1^2\Delta_a + k_2\omega_m, \quad k_{12} = \omega_b\omega_m - \gamma_m^2 + \tilde{\Delta}_m^2,$$
$$k_{13} = \omega_b\omega_m + 16k_1,$$
$$k_{14} = g^2G_1^2\Delta_a\omega_b - \omega_b\omega_m\left(\Delta_a^4 - k_4\right) + \Delta_a^3\left(\Delta_a\left(\gamma_m^2 - \Delta_m^2\right) + 2g^2\Delta_m\right) + k_4\gamma_b^2,$$
$$k_{15} = -3c_2\omega_b + 2k_1\omega_m + 8k_4,$$
$$k_{16} = \omega_b(k_3\omega_m - 5c_2) + k_1\gamma_b^2 + 2k_4.$$

Equations (A4)–(A12) ensure the cavity-magnomechanical system stability.

[1] T. Baumgratz, M. Cramer, and M. B. Plenio, Quantifying coherence, Phys. Rev. Lett. **113**, 140401 (2014).

[2] D. Girolami, Observable measure of quantum coherence in finite dimensional systems, Phys. Rev. Lett. **113**, 170401 (2014).

[3] K.-D. Wu, A. Streltsov, B. Regula, G.-Y. Xiang, C.-F. Li, and G.-C. Guo, Experimental progress on quantum coherence: detection, quantification, and manipulation, Adv. Quantum Technol. **4**, 2100040 (2021).

[4] E. Chitambar and G. Gour, Critical examination of incoherent operations and a physically consistent resource theory of quantum coherence, Phys. Rev. Lett. **117**, 030401 (2016).

[5] A. Winter and D. Yang, Operational resource theory of coherence, Phys. Rev. Lett. **116**, 120404 (2016).

[6] A. Streltsov, G. Adesso, and M. B. Plenio, Colloquium: Quantum coherence as a resource, Rev. Mod. Phys. **89**, 041003 (2017).

[7] M.-L. Hu, X. Hu, J. Wang, Y. Peng, Y.-R. Zhang, and H. Fan, Quantum coherence and geometric quantum discord, Phys. Rep. **762**, 1 (2018).

[8] F. Pan, L. Qiu, and Z. Liu, The complementarity relations of quantum coherence in quantum information processing, Sci. Rep. **7**, 43919 (2017).

[9] B. Fan, A. Samanta, and A. M. García-García, Tuning superinductors by quantum coherence effects for enhancing quantum computing, Phys. Rev. Lett. **130**, 047001 (2023).

[10] C. Weedbrook, S. Pirandola, R. García-Patrón, N. J. Cerf, T. C. Ralph, J. H. Shapiro, and S. Lloyd, Gaussian quantum information, Rev. Mod. Phys. **84**, 621 (2012).

[11] J. Roßnagel, O. Abah, F. Schmidt-Kaler, K. Singer, and E. Lutz, Nanoscale heat engine beyond the Carnot limit, Phys. Rev. Lett. **112**, 030602 (2014).

[12] J. Åberg, Catalytic coherence, Phys. Rev. Lett. **113**, 150402 (2014).

[13] V. Narasimhachar and G. Gour, Low-temperature thermodynamics with quantum coherence, Nat. Commun. **6**, 7689 (2015).

[14] G. Gour, Role of quantum coherence in thermodynamics, PRX Quantum **3**, 040323 (2022).

[15] M. Lostaglio, D. Jennings, and T. Rudolph, Description of quantum coherence in thermodynamic processes requires constraints beyond free energy, Nat. Commun. **6**, 6383 (2015).
[16] G. S. Engel, T. R. Calhoun, E. L. Read, T.-K. Ahn, T. Mančal, Y.-C. Cheng, R. E. Blankenship, and G. R. Fleming, Evidence for wavelike energy transfer through quantum coherence in photosynthetic systems, Nature (London) **446**, 782 (2007).
[17] N. Lambert, Y.-N. Chen, Y.-C. Cheng, C.-M. Li, G.-Y. Chen, and F. Nori, Quantum biology, Nat. Phys. **9**, 10 (2013).
[18] L. Mandel and E. Wolf, *Optical Coherence and Quantum Optics* (Cambridge University Press, Cambridge, 1995).
[19] J. K. Asbóth, J. Calsamiglia, and H. Ritsch, Computable measure of nonclassicality for light, Phys. Rev. Lett. **94**, 173602 (2005).
[20] W. Vogel and J. Sperling, Unified quantification of nonclassicality and entanglement, Phys. Rev. A **89**, 052302 (2014).
[21] M. Mraz, J. Sperling, W. Vogel, and B. Hage, Witnessing the degree of nonclassicality of light, Phys. Rev. A **90**, 033812 (2014).
[22] A. Castellini, R. Lo Franco, L. Lami, A. Winter, G. Adesso, and G. Compagno, Indistinguishability-enabled coherence for quantum metrology, Phys. Rev. A **100**, 012308 (2019).
[23] H. Kwon, K. C. Tan, T. Volkoff, and H. Jeong, Nonclassicality as a quantifiable resource for quantum metrology, Phys. Rev. Lett. **122**, 040503 (2019).
[24] J. Xu, Quantifying coherence of Gaussian states, Phys. Rev. A **93**, 032111 (2016).
[25] Y.-R. Zhang, L.-H. Shao, Y. Li, and H. Fan, Quantifying coherence in infinite-dimensional systems, Phys. Rev. A **93**, 012334 (2016).
[26] E. A. Donley, N. R. Claussen, S. T. Thompson, and C. E. Wieman, Atom–molecule coherence in a Bose-Einstein condensate, Nature (London) **417**, 529 (2002).
[27] E. W. Hagley, L. Deng, M. Kozuma, M. Trippenbach, Y. B. Band, M. Edwards, M. Doery, P. S. Julienne, K. Helmerson, S. L. Rolston, W. D. Phillips *et al.*, Measurement of the coherence of a Bose-Einstein condensate, Phys. Rev. Lett. **83**, 3112 (1999).
[28] A. Shcherbakova, K. Fedorov, K. Shulga, V. Ryazanov, V. Bolginov, V. Oboznov, S. Egorov, V. Shkolnikov, M. Wolf, D. Beckmann *et al.*, Fabrication and measurements of hybrid Nb/Al Josephson junctions and flux qubits with π-shifters, Supercond. Sci. Technol. **28**, 025009 (2015).
[29] Y. Shalibo, Y. Rofe, D. Shwa, F. Zeides, M. Neeley, J. M. Martinis, and N. Katz, Lifetime and coherence of two-level defects in a Josephson junction, Phys. Rev. Lett. **105**, 177001 (2010).
[30] F. Fröwis, B. Yadin, and N. Gisin, Insufficiency of avoided crossings for witnessing large-scale quantum coherence in flux qubits, Phys. Rev. A **97**, 042103 (2018).
[31] Q. Zheng, J. Xu, Y. Yao, and Y. Li, Detecting macroscopic quantum coherence with a cavity optomechanical system, Phys. Rev. A **94**, 052314 (2016).
[32] X. Li, W. Nie, A. Chen, and Y. Lan, Macroscopic quantum coherence and mechanical squeezing of a graphene sheet, Phys. Rev. A **96**, 063819 (2017).
[33] G. Li, W. Nie, X. Li, M. Li, A. Chen, and Y. Lan, Quantum coherence transfer between an optical cavity and mechanical resonators, Sci. China Phys. Mech. Astron. **62**, 100311 (2019).
[34] A. Kundu, C. Jin, and J.-X. Peng, Study of the optical response and coherence of a quadratically coupled optomechanical system, Phys. Scr. **96**, 065102 (2021).
[35] L. Jin, J.-X. Peng, Q.-Z. Yuan, and X.-L. Feng, Macroscopic quantum coherence in a spinning optomechanical system, Opt. Express **29**, 41191 (2021).
[36] J.-X. Peng, C. Jin, L. Jin, and Z.-X. Liu, Quantum coherence regulated by nanoparticles in a whispering-gallery-mode microresonator, Ann. Phys. **533**, 2100210 (2021).
[37] S. Singh, J.-X. Peng, M. Asjad, and M. Mazaheri, Entanglement and coherence in a hybrid Laguerre-Gaussian rotating cavity optomechanical system with two-level atoms, J. Phys. B: At. Mol. Opt. Phys. **54**, 215502 (2021).
[38] H. Kang, D. Han, N. Wang, Y. Liu, S. Hao, and X. Su, Experimental demonstration of robustness of Gaussian quantum coherence, Photon. Res. **9**, 1330 (2021).
[39] C. Marquardt, U. L. Andersen, G. Leuchs, Y. Takeno, M. Yukawa, H. Yonezawa, and A. Furusawa, Experimental demonstration of macroscopic quantum coherence in Gaussian states, Phys. Rev. A **76**, 030101(R) (2007).
[40] A. Z. Goldberg, P. De La Hoz, G. Björk, A. B. Klimov, M. Grassl, G. Leuchs, and L. L. Sánchez-Soto, Quantum concepts in optical polarization, Adv. Opt. Photon. **13**, 1 (2021).
[41] C. Rosales-Guzmán, B. Ndagano, and A. Forbes, A review of complex vector light fields and their applications, J. Opt. **20**, 123001 (2018).
[42] J. Chen, C. Wan, and Q. Zhan, Vectorial optical fields: recent advances and future prospects, Sci. Bull. **63**, 54 (2018).
[43] J. Ahn, Z. Xu, J. Bang, Y.-H. Deng, T. M. Hoang, Q. Han, R.-M. Ma, and T. Li, Optically levitated nanodumbbell torsion balance and GHz nanomechanical rotor, Phys. Rev. Lett. **121**, 033603 (2018).
[44] W. Liu, D. Dong, H. Yang, Q. Gong, and K. Shi, Robust and high-speed rotation control in optical tweezers by using polarization synthesis based on heterodyne interference, Opto-Electron. Adv. **3**, 200022 (2020).
[45] F. Walter, G. Li, C. Meier, S. Zhang, and T. Zentgraf, Ultrathin nonlinear metasurface for optical image encoding, Nano Lett. **17**, 3171 (2017).
[46] Y. Kozawa and S. Sato, Optical trapping of micrometer-sized dielectric particles by cylindrical vector beams, Opt. Express **18**, 10828 (2010).
[47] R. Chen, K. Agarwal, C. J. Sheppard, and X. Chen, Imaging using cylindrical vector beams in a high-numerical-aperture microscopy system, Opt. Lett. **38**, 3111 (2013).
[48] M. Xian, Y. Xu, X. Ouyang, Y. Cao, S. Lan, and X. Li, Segmented cylindrical vector beams for massively-encoded optical data storage, Sci. Bull. **65**, 2072 (2020).
[49] M. Neugebauer, P. Woźniak, A. Bag, G. Leuchs, and P. Banzer, Polarization-controlled directional scattering for nanoscopic position sensing, Nat. Commun. **7**, 11286 (2016).
[50] X. Zhang, Q.-T. Cao, Z. Wang, Y.-X. Liu, C.-W. Qiu, L. Yang, Q. Gong, and Y.-F. Xiao, Symmetry-breaking-induced nonlinear optics at a microcavity surface, Nat. Photon. **13**, 21 (2019).
[51] F. Cardano and L. Marrucci, Spin–orbit photonics, Nat. Photon. **9**, 776 (2015).
[52] K. Y. Bliokh, F. J. Rodríguez-Fortuño, F. Nori, and A. V. Zayats, Spin–orbit interactions of light, Nat. Photon. **9**, 796 (2015).

[53] H. Xiong, Y.-M. Huang, L.-L. Wan, and Y. Wu, Vector cavity optomechanics in the parameter configuration of optomechanically induced transparency, Phys. Rev. A **94**, 013816 (2016).
[54] Y. Li, Y.-F. Jiao, J.-X. Liu, A. Miranowicz, Y.-L. Zuo, L.-M. Kuang, and H. Jing, Vector optomechanical entanglement, Nanophotonics **11**, 67 (2021).
[55] B. Bhoi and S.-K. Kim, Photon-magnon coupling: historical perspective, status, and future directions, Solid State Phys. **70**, 1 (2019).
[56] H. Yuan, Y. Cao, A. Kamra, R. A. Duine, and P. Yan, Quantum magnonics: When magnon spintronics meets quantum information science, Phys. Rep. **965**, 1 (2022).
[57] B. Z. Rameshti, S. V. Kusminskiy, J. A. Haigh, K. Usami, D. Lachance-Quirion, Y. Nakamura, C.-M. Hu, H. X. Tang, G. E. Bauer, and Y. M. Blanter, Cavity magnonics, Phys. Rep. **979**, 1 (2022).
[58] X. Zhang, C.-L. Zou, L. Jiang, and H. X. Tang, Cavity magnomechanics, Sci. Adv. **2**, e1501286 (2016).
[59] J.-M. Raimond, M. Brune, and S. Haroche, Manipulating quantum entanglement with atoms and photons in a cavity, Rev. Mod. Phys. **73**, 565 (2001).
[60] G. S. Agarwal, Vacuum-field Rabi splittings in microwave absorption by Rydberg atoms in a cavity, Phys. Rev. Lett. **53**, 1732 (1984).
[61] Y.-H. Lien, G. Barontini, M. Scheucher, M. Mergenthaler, J. Goldwin, and E. A. Hinds, Observing coherence effects in an overdamped quantum system, Nat. Commun. **7**, 13933 (2016).
[62] B. Yao, Y. Gui, J. Rao, S. Kaur, X. Chen, W. Lu, Y. Xiao, H. Guo, K.-P. Marzlin, and C.-M. Hu, Cooperative polariton dynamics in feedback-coupled cavities, Nat. Commun. **8**, 1437 (2017).
[63] J. Li, S.-Y. Zhu, and G. S. Agarwal, Magnon-photon-phonon entanglement in cavity magnomechanics, Phys. Rev. Lett. **121**, 203601 (2018).
[64] J. Li, S.-Y. Zhu, and G. S. Agarwal, Squeezed states of magnons and phonons in cavity magnomechanics, Phys. Rev. A **99**, 021801(R) (2019).
[65] Q. Guo, D. Xu, J. Cheng, H. Tan, and J. Li, Magnon squeezing by two-tone driving of a qubit in cavity-magnon-qubit systems, Phys. Rev. A **108**, 063703 (2023).
[66] J. Li and S.-Y. Zhu, Entangling two magnon modes via magnetostrictive interaction, New J. Phys. **21**, 085001 (2019).
[67] F.-X. Sun, S.-S. Zheng, Y. Xiao, Q. Gong, Q. He, and K. Xia, Remote generation of magnon Schrödinger cat state via magnon-photon entanglement, Phys. Rev. Lett. **127**, 087203 (2021).
[68] M. Yu, H. Shen, and J. Li, Magnetostrictively induced stationary entanglement between two microwave fields, Phys. Rev. Lett. **124**, 213604 (2020).
[69] J. Li, Y.-P. Wang, J.-Q. You, and S.-Y. Zhu, Squeezing microwaves by magnetostriction, Natl. Sci. Rev. **10**, nwac247 (2023).
[70] H. Qian, X. Zuo, Z.-Y. Fan, J. Cheng, and J. Li, Strong squeezing of microwave output fields via reservoir-engineered cavity magnomechanics, Phys. Rev. A **109**, 013704 (2024).
[71] M. Asjad, J. Li, S.-Y. Zhu, and J. You, Magnon squeezing enhanced ground-state cooling in cavity magnomechanics, Fundam. Res. **3**, 3 (2023).
[72] S. Sharma, Y. M. Blanter, and G. E. Bauer, Optical cooling of magnons, Phys. Rev. Lett. **121**, 087205 (2018).
[73] Y.-P. Wang, G.-Q. Zhang, D. Zhang, T.-F. Li, C.-M. Hu, and J. Q. You, Bistability of cavity magnon polaritons, Phys. Rev. Lett. **120**, 057202 (2018).
[74] R.-C. Shen, J. Li, Z.-Y. Fan, Y.-P. Wang, and J. Q. You, Mechanical bistability in Kerr-modified cavity magnomechanics, Phys. Rev. Lett. **129**, 123601 (2022).
[75] C.-Z. Chai, X.-X. Hu, C.-L. Zou, G.-C. Guo, and C.-H. Dong, Thermal bistability of magnon in yttrium iron garnet microspheres, Appl. Phys. Lett. **114**, 021101 (2019).
[76] H. Pan, Y. Yang, Z. H. An, and C.-M. Hu, Bistability in dissipatively coupled cavity magnonics, Phys. Rev. B **106**, 054425 (2022).
[77] G. Zhang, Y. Wang, and J. You, Theory of the magnon Kerr effect in cavity magnonics, Sci. China Phys. Mech. Astron. **62**, 987511 (2019).
[78] Z.-X. Liu, H. Xiong, and Y. Wu, Magnon blockade in a hybrid ferromagnet-superconductor quantum system, Phys. Rev. B **100**, 134421 (2019).
[79] Y. Wang, W. Xiong, Z. Xu, G.-Q. Zhang, and J.-Q. You, Dissipation-induced nonreciprocal magnon blockade in a magnon-based hybrid system, Sci. China Phys. Mech. Astron. **65**, 260314 (2022).
[80] J.-K. Xie, S.-L. Ma, and F.-L. Li, Quantum-interference-enhanced magnon blockade in an yttrium-iron-garnet sphere coupled to superconducting circuits, Phys. Rev. A **101**, 042331 (2020).
[81] K. Wu, W.-X. Zhong, G.-L. Cheng, and A.-X. Chen, Phase-controlled multimagnon blockade and magnon-induced tunneling in a hybrid superconducting system, Phys. Rev. A **103**, 052411 (2021).
[82] H. Xie, L.-W. He, X. Shang, G.-W. Lin, and X.-M. Lin, Nonreciprocal photon blockade in cavity optomagnonics, Phys. Rev. A **106**, 053707 (2022).
[83] Z. Wang, H. Y. Yuan, Y. Cao, and P. Yan, Twisted magnon frequency comb and Penrose superradiance, Phys. Rev. Lett. **129**, 107203 (2022).
[84] T.-X. Lu, H. Zhang, Q. Zhang, and H. Jing, Exceptional-point-engineered cavity magnomechanics, Phys. Rev. A **103**, 063708 (2021).
[85] Z.-X. Liu, H. Xiong, M.-Y. Wu, and Y.-Q. Li, Absorption of magnons in dispersively coupled hybrid quantum systems, Phys. Rev. A **103**, 063702 (2021).
[86] C. Kong, H. Xiong, and Y. Wu, Magnon-induced nonreciprocity based on the magnon kerr effect, Phys. Rev. Appl. **12**, 034001 (2019).
[87] H. Y. Yuan, J. Xie, and R. A. Duine, Magnon bundle in a strongly dissipative magnet, Phys. Rev. Appl. **19**, 064070 (2023).
[88] J.-K. Xie, S.-L. Ma, Y.-L. Ren, S.-Y. Gao, and F.-L. Li, Chiral cavity-magnonic system for the unidirectional emission of a tunable squeezed microwave field, Phys. Rev. A **108**, 033701 (2023).
[89] H. Xiong, Magnonic frequency combs based on the resonantly enhanced magnetostrictive effect, Fundam. Res. **3**, 8 (2023).
[90] T. Wang, W. Zhang, J. Cao, and H.-F. Wang, Exceptional-point-engineered phonon laser in a cavity magnomechanical system, New J. Phys. **25**, 083045 (2023).
[91] Z.-X. Liu and Y.-Q. Li, Optomagnonic frequency combs, Photon. Res. **10**, 2786 (2022).

[92] S.-Y. Guan, H.-F. Wang, and X. Yi, Cooperative-effect-induced one-way steering in open cavity magnonics, npj Quantum Inf. **8**, 102 (2022).
[93] T.-A. Zheng, Y. Zheng, L. Wang, and C.-G. Liao, Dissipative generation of significant amount of photon-phonon asymmetric steering in magnomechanical interfaces, EPJ Quantum Technol. **10**, 19 (2023).
[94] J. Li, Y.-P. Wang, W.-J. Wu, S.-Y. Zhu, and J. Q. You, Quantum network with magnonic and mechanical nodes, PRX Quantum **2**, 040344 (2021).
[95] B. Sarma, T. Busch, and J. Twamley, Cavity magnomechanical storage and retrieval of quantum states, New J. Phys. **23**, 043041 (2021).
[96] Z.-Y. Fan, R.-C. Shen, Y.-P. Wang, J. Li, and J. Q. You, Optical sensing of magnons via the magnetoelastic displacement, Phys. Rev. A **105**, 033507 (2022).
[97] Z. Jin, X. Yao, Z. Wang, H. Y. Yuan, Z. Zeng, W. Wang, Y. Cao, and P. Yan, Nonlinear topological magnon spin Hall effect, Phys. Rev. Lett. **131**, 166704 (2023).
[98] Y.-L. Ren, S.-L. Ma, and F.-L. Li, Chiral coupling between a ferromagnetic magnon and a superconducting qubit, Phys. Rev. A **106**, 053714 (2022).
[99] H. Y. Yuan, R. Lavrijsen, and R. A. Duine, Unidirectional magnetic coupling induced by chiral interaction and nonlocal damping, Phys. Rev. B **107**, 024418 (2023).
[100] Z.-Y. Fan, H. Qian, X. Zuo, and J. Li, Entangling ferrimagnetic magnons with an atomic ensemble via optomagnomechanics, Phys. Rev. A **108**, 023501 (2023).
[101] H. Qian, Z.-Y. Fan, and J. Li, Entangling mechanical vibrations of two massive ferrimagnets by fully exploiting the nonlinearity of magnetostriction, Quantum Sci. Technol. **8**, 015022 (2022).
[102] Z.-Y. Fan, H. Qian, and J. Li, Stationary optomagnonic entanglement and magnon-to-optics quantum state transfer via opto-magnomechanics, Quantum Sci. Technol. **8**, 015014 (2022).
[103] W.-J. Wu, Y.-P. Wang, J.-Z. Wu, J. Li, and J. Q. You, Remote magnon entanglement between two massive ferrimagnetic spheres via cavity optomagnonics, Phys. Rev. A **104**, 023711 (2021).
[104] H. Tan and J. Li, Einstein-podolsky-rosen entanglement and asymmetric steering between distant macroscopic mechanical and magnonic systems, Phys. Rev. Res. **3**, 013192 (2021).
[105] J. Li and S. Gröblacher, Entangling the vibrational modes of two massive ferromagnetic spheres using cavity magnomechanics, Quantum Sci. Technol. **6**, 024005 (2021).
[106] W. Qiu, X. Cheng, A. Chen, Y. Lan, and W. Nie, Controlling quantum coherence and entanglement in cavity magnomechanical systems, Phys. Rev. A **105**, 063718 (2022).
[107] M. Yu, S.-Y. Zhu, and J. Li, Macroscopic entanglement of two magnon modes via quantum correlated microwave fields, J. Phys. B: At. Mol. Opt. Phys. **53**, 065402 (2020).
[108] Z. Zhang, M. O. Scully, and G. S. Agarwal, Quantum entanglement between two magnon modes via kerr nonlinearity driven far from equilibrium, Phys. Rev. Res. **1**, 023021 (2019).
[109] H. Y. Yuan, S. Zheng, Z. Ficek, Q. Y. He, and M.-H. Yung, Enhancement of magnon-magnon entanglement inside a cavity, Phys. Rev. B **101**, 014419 (2020).
[110] A. Sohail, R. Ahmed, J.-X. Peng, A. Shahzad, and S. Singh, Enhanced entanglement via magnon squeezing in a two-cavity magnomechanical system, JOSA B **40**, 1359 (2023).
[111] H.-J. Cheng, S.-J. Zhou, J.-X. Peng, A. Kundu, H.-X. Li, L. Jin, and X.-L. Feng, Tripartite entanglement in a Laguerre-Gaussian rotational-cavity system with an yttrium iron garnet sphere, JOSA B **38**, 285 (2021).
[112] G. Zhao, Y. Wang, and X.-F. Qian, Driven dissipative quantum dynamics in a cavity magnon-polariton system, Phys. Rev. B **104**, 134423 (2021).
[113] K. Ullah, M. T. Naseem, and Ö. E. Müstecaplıoğlu, Tunable multiwindow magnomechanically induced transparency, fano resonances, and slow-to-fast light conversion, Phys. Rev. A **102**, 033721 (2020).
[114] A. Melloni, F. Morichetti, and M. Martinelli, Polarization conversion in ring resonator phase shifters, Opt. Lett. **29**, 2785 (2004).
[115] G. S. Agarwal, *Quantum Optics* (Cambridge University Press, Cambridge, 2012).
[116] A. Rivas and S. F. Huelga, *Open Quantum Systems* (Springer, Berlin, 2012), Vol. 10.
[117] C. Gardiner and P. Zoller, *Quantum Noise: A Handbook of Markovian and Non-Markovian Quantum Stochastic Methods with Applications to Quantum Optics* (Springer Science & Business Media, New York, 2004).
[118] E. X. DeJesus and C. Kaufman, Routh-hurwitz criterion in the examination of eigenvalues of a system of nonlinear ordinary differential equations, Phys. Rev. A **35**, 5288 (1987).
[119] D. Vitali, S. Gigan, A. Ferreira, H. R. Böhm, P. Tombesi, A. Guerreiro, V. Vedral, A. Zeilinger, and M. Aspelmeyer, Optomechanical entanglement between a movable mirror and a cavity field, Phys. Rev. Lett. **98**, 030405 (2007).
[120] E. Alp, W. Sturhahn, and T. Toellner, Polarizer–analyzer optics, Hyperfine Interact. **125**, 45 (2000).
[121] C. A. Potts, E. Varga, V. A. S. V. Bittencourt, S. V. Kusminskiy, and J. P. Davis, Dynamical backaction magnomechanics, Phys. Rev. X **11**, 031053 (2021).
[122] X.-B. Yan, Z.-J. Deng, X.-D. Tian, and J.-H. Wu, Entanglement optimization of filtered output fields in cavity optomechanics, Opt. Express **27**, 24393 (2019).